Surface-Enhanced Raman Spectroscopy Integrated Centrifugal Microfluidics Platform

Durucan, Onur

Publication date:
2018

Document Version
Publisher's PDF, also known as Version of record

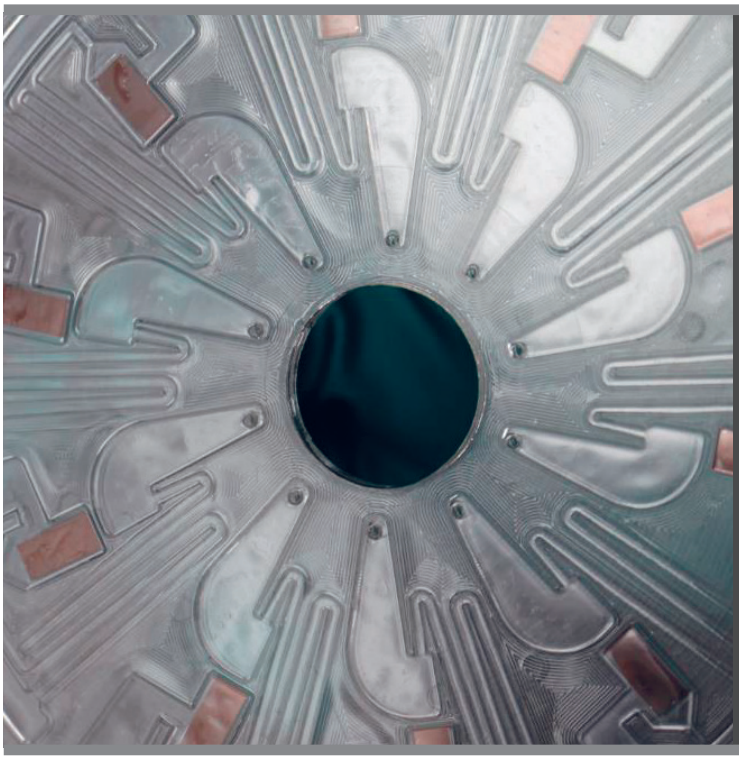

Surface-Enhanced Raman Spectroscopy Integrated Centrifugal Microfluidics Platform

Onur Durucan
PhD Thesis January 2018

DTU Nanotech
Department of Micro- and Nanotechnology

DTU Nanotech
Department of Micro- and Nanotechnology

DTU

Surface-Enhanced Raman Spectroscopy Integrated Centrifugal Microfluidics Platform

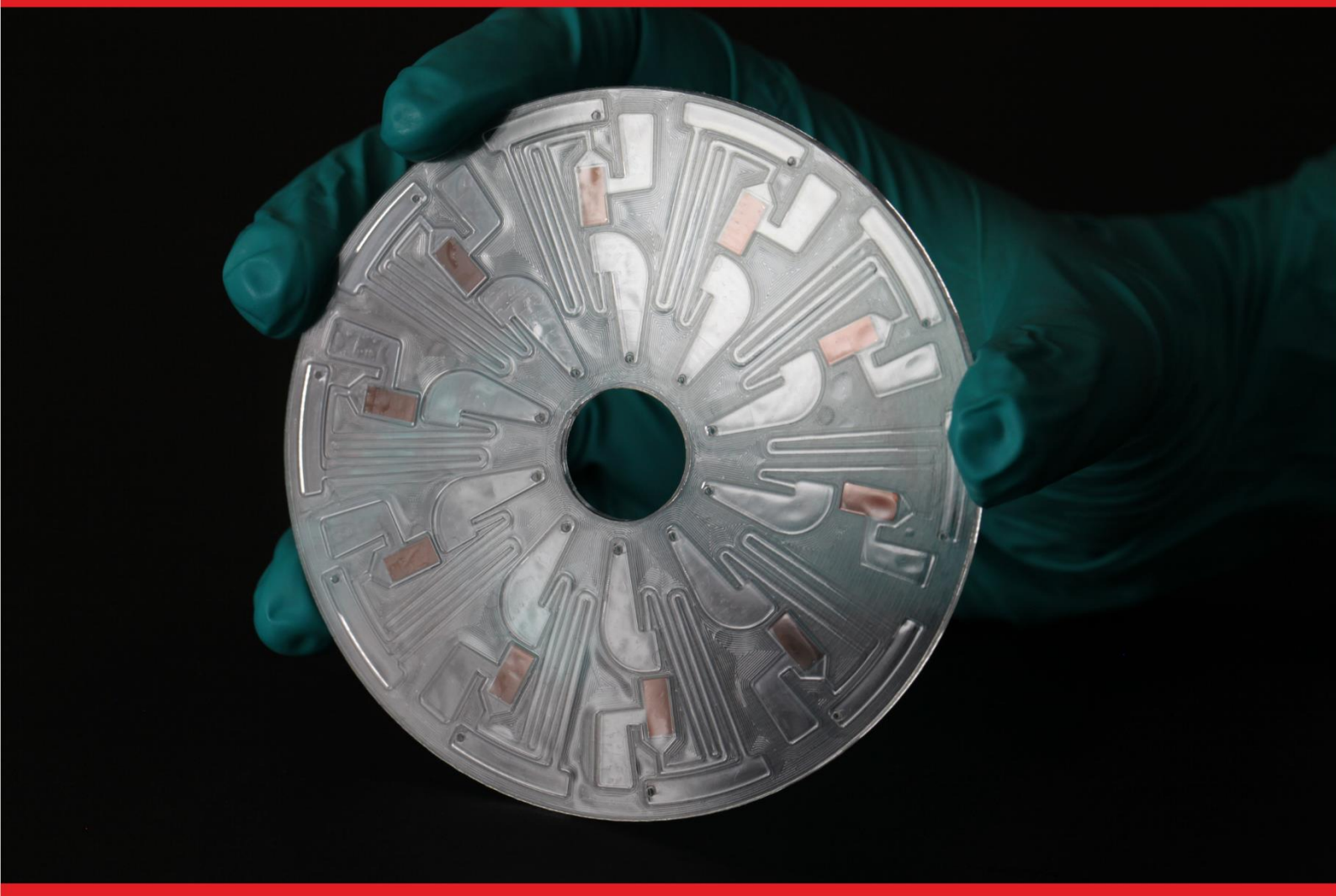

Ph.D. Thesis

Onur Durucan

January 2018

SURFACE-ENHANCED RAMAN SPECTROSCOPY INTEGRATED CENTRIFUGAL MICROFLUIDICS PLATFORM

A Thesis

Presented to

The Academic Faculty

by

Onur Durucan

In Partial Fulfilment

of the Requirements for the

Ph.D. Degree in the

Department of Micro- and Nanotechnology

Technical University of Denmark

January 2018

SURFACE-ENHANCED RAMAN SPECTROSCOPY INTEGRATED CENTRIFUGAL MICROFLUIDICS PLATFORM

Main Supervisor:

Professor Anja Boisen
Department of Micro- and Nanotechnology
Technical University of Denmark

Co-supervisor:

Associate Professor Tomas Rindzevicius
Department of Micro- and Nanotechnology
Technical University of Denmark

Co-supervisor:

Senior Researcher Michael Stenbæk Schmidt
Department of Micro- and Nanotechnology
Technical University of Denmark

Co-supervisor:

Dr. Marco Matteucci
Production Manager
NIL Technology ApS

PREFACE

In this thesis, the summary of research activities conducted throughout the PhD employment from 15th of January 2015 at the Nanoprobes research group (Department of Micro- and Nanotechnology, Technical University of Denmark) is presented. The PhD project was part of the HERMES-High Exponential Rise in Miniaturized cantilever-like Sensing project founded by European Research Council (ERC), grant no. 320535.

ACKNOWLEDGEMENTS

First of all, I would like to thank my supervisors Professor Anja Boisen, Associate Professor Tomas Rindzevicius, Senior Researcher Michael Stenbæk Schmidt and Dr. Marco Matteucci for their continuous support and guidance throughout my PhD study. I have really enjoyed the process of my PhD study. There was always somebody in my supervisor team who would suggest ideas and mentor me to overcome toughest obstacles that came across the project. I am very grateful to Associate Professor Tomas Rindzevicius and Senior Researcher Michael Stenbæk Schmidt for countless times of scientific discussions which provided insights and greatly assisted the research. I have learned a lot from Professor Anja Boisen, especially about the effective communication, educational development and personal problem-solving skills. Also, I appreciate my former supervisor Dr. Robert Burger, who is now a part of a start-up company, for introducing me to the centrifugal microfluidics platform. His supervision and shared knowledge during the first year have greatly facilitated the experimental studies and provided me deep conceptual understanding of microfluidics.

I would like to express my gratitude to the Nanoprobes group which I was part of during the PhD study for a collaborative, friendly and positive research environment. On this account, I greatly appreciate my research collaborators and colleagues, especially Postdoc. Kaiyu Wu, Dr. Kuldeep Sanger, Dr. Anil Haraksingh Thilsted, Lidia Morelli, Marlitt Viehrig. Also, Rokon Uddin, Lukas Vaut, Postdoc. Oleksii Ilchenko, Zarmeena Abid for numerous scientific discussions, expertise and support throughout the project.

Lastly, I want to thank my family and Yana for their great support. They have always kept me positive and motivated and encouraged me to achieve my goals.

Onur Durucan
January 2018

ABSTRACT

This PhD thesis demonstrates (i) centrifugal microfluidics disc platform integrated with Au capped nanopillar (NP) substrates for surface-enhanced Raman spectroscopy (SERS) based sensing, and (ii) novel sample analysis concepts achieved by synergistical combination of sensing techniques and miniaturized fluid handling devices for facile quantitative and qualitative analysis of real-life sample matrices.

A nanofiltration approach based on a wicking (wetting) phenomenon of fluids on nanostructured surfaces was introduced. The method provides purification of complex suspensions by passing it through dense array of NP structures. Furthermore, the wicking assisted nanofiltration procedure was accomplished in centrifugal microfluidics platform and as a result additional sample purification was achieved through the centrifugation process. In this way, the Au coated NP substrate was utilized as nanofilter and SERS active surface at the same time.

To evaluate the efficiency of the nanofiltration technique, a well-known application case, detection of toxic melamine molecules in milk, was selected. According to the statistical SERS map analysis conducted on the purified sample region of the NP surface (2×4 mm^2), the spectral response for melamine was 14 times higher as compared to the immersed and non-purified part of the chip. The quantitative study of melamine content with respect to the averaged peak intensity at 687 cm^{-1} was in accordance with characteristic Langmuir adsorption curve behavior and the detection limit was estimated to be 10 parts per million (ppm).

The wicking based fluid sample transport was further investigated for simultaneous detection of multiple components in human urine solutions. Using the surface sensitivity of the SERS technique, affinity based chromatographic separation of urine compounds such as creatinine, uric acid and urea was achieved. Additionally, a unique and novel quantification procedure based on spectral profiles was presented.

Lastly, an alternative sensing approach was carried out using Au coated NP like structures on fused silica. By combining the advantages of electrochemical (EC) systems for quantitative analysis and the molecular specificity of SERS, a proof-of-concept study on detection of paracetamol in phosphate-buffered saline (PBS) was performed.

RESUMÉ

I denne ph.d.afhandling demonstreres: (i) En såkaldt 'centrifugal microfluid disc' platform med integreret sensor substrat ('Au capped nanopillar substrate') til surface-enhanced Raman spektroskopi (SERS). Og (ii) et nyt analysekoncept hvor sensor-teknologi og en teknik til håndtering af væske kombineres til en enkel metode til kvantitativ og kvalitativ analyse af komplicerede prøver.

Der introduceres en metode til nanofiltrering baseret på nanostrukturerede overfladers evne til at opsuge væske. Med denne metode kan komplekse opløsninger oprenses ved at passere et tæt array af nanostrukturer ('Au capped nanopillars'). Denne metode for nanofiltrering er integreret på førnævnte 'centrifugal microfluidic platform' og hermed opnås yderligere oprensning af prøven gennem centrifugeringsprocessen. På denne måde bruges det integrerede sensor substrat ('Au capped nanopillar substrate') både som filter i oprensningen af prøven og som SERS substrat til detektion, på samme tid.

For at evaluere effektiviteten af metoden til nanofiltrering, er der valgt en velkendt anvendelse, nemlig detektion af giftig melamin i mælk. Ifølge SERS analysen var responsen for melamin på den del af substratet hvor prøven havde passeret nanostrukturen 14 gange højere end på den del der havde været nedsænket direkte i prøven. Den kvantitative analyse af mængden af melamin i forhold til den gennemsnitlige peak intensitet på 687 cm^{-1}, var i overensstemmelse med den karakteristiske Langmuir adsorption og detektionsgrænsen er estimeret til 10 parts per million (ppm).

Metoden til nanofiltrering er undersøgt yderligere til samtidig detektion af flere forskellige stoffer i en opløsning af menneskelig urin. Ved brug af SERS teknikkens overfladesensitivitet opnås affinitetsbaseret kromatografi af stoffer i urin såsom creatinine, urinsyre og urea. Ydermere, præsenteres der en unik, ny procedure til kvantificering baseret på stoffernes profiler i spektrene.

Afslutningsvist er de samme nanostrukturer ('Au coated nanopillars') på glas, brugt som en alternativ sensor. Ved at kombinere fordelene ved elektrokemiske systemer til kvantitativ analyse og den molekylære specificitet fra SERS, er der udført et 'proof-of-concept' studie på detektion af paracetamol i 'phosphate-buffered saline (PBS)'.

TABLE OF CONTENTS

LIST OF FIGURES

LIST OF ABBREVIATIONS

RS – Raman Scattering

EM – Electromagnetic

SERS – Surface-enhanced Raman spectroscopy

EC – Electrochemistry

LSP – Localized surface plasmon

FDTD – Finite-difference time-domain

EF – Enhancement factor

MEF – Metal-enhanced fluorescence

NP – Nanopillar

RIE – Reactive ion etching

SEM – Scanning electron microscopy

PMMA – Poly (methyl methacrylate)

PSA – Pressure sensitive adhesive

CV – Cyclic voltammogram

WE – Working electrode

CE – Counter electrode

RE – Reference electrode

Ag – Silver

Au – Gold

Al – Alluminum

Cu – Copper

Si – Silicon

SiO_2 – Fused Silica

SF_6 – Sulphur hexafluoride

O_2 – Oxygen

1 INTRODUCTION

The discovery of the surface-enhanced Raman scattering (RS) phenomenon can be dated back to 1973, when an enormous Raman signal increase was observed for pyridine molecules on electrochemically roughened Ag surface[1]. Today surface-enhanced Raman spectroscopy (SERS) is a well-established and powerful technique for studying molecular vibrations. The SERS method enables detection of tremendously enhanced RS signals from molecules that are situated in the close vicinity (within a few nm) of the plasmonic nanostructure surface[2,3]. Similar to the Raman spectroscopy technique, the analysed molecular species are identified through their molecular fingerprint spectra. It is well established that the boost in the RS signal is obtained via (1) local concentration of the incident light at the nanoscale regions ("hot-spots") promoted by the localized surface plasmon (LSP) excitation[4,5] (electromagnetic enhancement), and (2) electronic band interaction between the analysed molecule and the metal surface (chemical enhancement)[6]. Some specific cases for SERS based detection of even single molecules have been already demonstrated[7–9].

Only in recent decade, with the technological advancements in controlled micro- and nanofabrication techniques, the SERS field started to gradually attract practical interest in research environment as well as outside lab implementations[10–16]. The main advantages of the SERS based systems are accounted for their molecular specificity, high sensitivity and fluorescence quenching effect[17,18]. It was shown in multiple studies that the SERS technique is suitable for examining the molecular reaction in electrochemistry (EC) processes[19,20], imaging and dynamic study of single molecule systems[21,22]. In

addition to that, a broad range of sensing applications on fluid and gaseous samples were developed for detection of toxins for environmental[23] and food safety research[24,25], pharmaceutical studies[26], and medical diagnostics[27,28]. As a result, the technical understanding behind the working mechanisms of the surface-enhanced RS effect and essential requirements for plasmonic surfaces were interrogated and presented in numerous theoretical and experimental reports. For developing reliable sensing applications, SERS substrates require the following: (i) the fabrication procedure of a SERS substrate should be scalable, reproducible and cost effective, (ii) display high ($>10^7$) and uniformly distributed ($>cm^2$) electromagnetic field enhancement factors (EF), and lastly (iii) applicable for a broad range of LSP resonance modes[15,16,29,30]. On that account, various highly ordered nanostructured SERS active surfaces with satisfactory SERS performance were developed using mostly lithography based techniques[31–33]. Despite all the progress in the SERS substrates fabrication field, current SERS sensing methodologies are not universal, lack efficiency and reproducibility for analysing complex, multicomponent real-life samples compared to e.g. existing techniques such as high-performance liquid chromatography (HPLC)[34,35], capillary electrophoresis[36,37] integrated detectors, lateral flow based assays[38,39] or traditional Raman spectroscopy[40,41].

The main technical challenge for SERS based detection of analyte molecules in complex media such as blood plasma, urine, saliva, milk, juice, waste water, etc. is related to their chemically rich environment[23,27,42]. Since the phenomenon is highly surface sensitive, an ideal SERS measurement is necessitating relatively pure sample environment on the active region. In general terms, macromolecular structures such as proteins, cells, fats tend to block electromagnetic “hot-spots” which significantly limits further SERS-based detection of analyte compounds[43]. Moreover, on some occasions the sample fluid may contain multiple molecular species with varying affinities towards nanostructured metal surface. Due to competitive binding of these different components

on a SERS active region[44], the limit of detection for distinct analyte species can be greatly reduced.

A number of sample pre-treatment and handling methods to overcome above mentioned practical issues for SERS based applications on complex suspensions have already been demonstrated. For example, functionalization of the SERS active surface[43], analytical liquid-liquid extraction technique[45,46], filtration on porous membranes[47,48], analyte enrichment procedures[49], integration of microfluidic devices[50–52] and incorporation of external chromatographic platforms such as HPLC and thin-layer chromatography (TLC)[53–55] are the most prominent sample handling techniques for SERS. Nevertheless, the current integrated SERS based platforms are application specific, time consuming, lack sensitivity or do not provide quantitative information.

1.1 Aim of the PhD Project

This PhD study is a part of the HERMES-High Exponential Rise in Miniaturized cantilever-like Sensing project funded by European Research Council (ERC). The main objective of the project is to solve fundamental challenges of SERS based sensing applications in real-life complex samples like blood, milk and saliva. To accomplish this, the SERS measurements ideally should be (i) reliable, (ii) sensitive, (iii) reproducible and (iv) high-throughput. These sensing characteristics can be achieved by utilizing high performance, nanopillar-based SERS substrates and controlled sample pre-treatment\deposition techniques. The state-of-the-art metal capped nanopillar (NP) SERS substrates developed by senior researcher Michael Stenbæk Schmidt in the Nanoprobes group are potentially suitable for practical applications. Thus, in this PhD project, the contribution of controlled sample pre-treatment and dosage techniques for SERS based sensing are examined, and the proof-of-concept studies are performed on the Au capped

NP arrays. Accordingly, these fluid manipulation steps are accomplished using a centrifugal microfluidics platform.

Specific objectives of the PhD project are the following: (i) design, optimize and fabricate polymeric centrifugal microfluidic discs for desired fluid handling steps, (ii) integrate the NP-based SERS active surfaces into the centrifugal microfluidics platform and (iii) demonstrate potential applicability of the integrated platform using well-known sensing examples in complex sample solutions. Lastly, it should be emphasized that the proposed solutions in the SERS based sensing system are aimed to be versatile, automated, free of human interaction, and more importantly without any surface functionalization.

1.2 Structure of the Thesis

This introductory part of the thesis (Chapter 1) is followed by 4 chapters that provide theoretical background for this PhD project. Namely, in Chapter 2 (Raman Effect), the fundamental concept behind the SERS phenomenon, inelastic light scattering effect (Raman scattering) for probing the vibrational modes of molecules is given. Further, the surface-enhancement of Raman scattering signal is elaborated through the electromagnetic enhancement mechanism in Chapter 3 (Surface-Enhanced Raman Scattering). The Au coated NP SERS substrates which have been utilized throughout the project are described in Chapter 4 (Plasmonic NP Structures). Lastly, the fluid handling platform, i.e. centrifugal microfluidics, is presented in Chapter 5 (Centrifugal Microfluidics). The results obtained during the PhD project are discussed in Chapters 6-8. In Chapter 6 (Nanopillar filters for SERS), a facile and simple method to eliminate macromolecular clusters through the wicking effect of fluids and detection of small analyte molecules in complex sample medium is described. The multicomponent analyte detection in chemically rich sample environment is introduced in Chapter 7 (NP

Structures for SERS Chromatography) using a similar technique as in Chapter 6. An alternative SERS based sensing approach is demonstrated in Chapter 8 (Dual-Functional EC and SERS Sensing). Here the two techniques, i.e. electrochemical detection and SERS based qualitative analysis, were implemented for sample analysis. Finally, conclusions and an overview of main achievements of the PhD project are summarized in Chapter 9 (Concluding Remarks).

References

(1) Fleischmann, M.; Hendra, P. J.; McQuillan, A. J. *Chem. Phys. Lett.* **1974**, *26* (2), 163–166.

(2) Otto, A.; Mrozek, I.; Grabhorn, H.; Akemann, W. *J. Phys. Condens. Matter* **1992**, *4* (5), 1143–1212.

(3) Kneipp, K.; Kneipp, H.; Itzkan, I.; Dasari, R. R.; Feld, M. S. *J. Phys. Condens. Matter* **2002**, *14* (18), 202.

(4) Campion, A.; Kambhampati, P. *Chem. Soc. Rev.* **1998**, *27* (4), 241.

(5) Stiles, P. L.; Dieringer, J. A.; Shah, N. C.; Van Duyne, R. P. *Annu. Rev. Anal. Chem.* **2008**, *1* (1), 601–626.

(6) Le Ru, E. C.; Blackie, E.; Meyer, M.; Etchegoin, P. G. *J. Phys. Chem. C* **2007**, *111* (37), 13794–13803.

(7) Camden, J. P.; Dieringer, J. A.; Wang, Y.; Masiello, D. J.; Marks, L. D.; Schatz, G. C.; Van Duyne, R. P. *J. Am. Chem. Soc.* **2008**, *130* (38), 12616–12617.

(8) Nie, S. *Science (80-.).* **1997**, *275* (5303), 1102–1106.

(9) Kneipp, K.; Wang, Y.; Kneipp, H.; Perelman, L. T.; Itzkan, I.; Dasari, R. R.; Feld, M. S. *Phys. Rev. Lett.* **1997**, *78* (9), 1667–1670.

(10) Haes, A. J.; Haynes, C. L.; McFarland, A. D.; Schatz, G. C.; Van Duyne, R. P.; Zou, S. *MRS Bull.* **2005**, *30* (5), 368–375.

(11) Cialla, D.; März, A.; Böhme, R.; Theil, F.; Weber, K.; Schmitt, M.; Popp, J. *Anal. Bioanal. Chem.* **2012**, *403* (1), 27–54.

(12) Petry, R.; Schmitt, M.; Popp, J. *ChemPhysChem* **2003**, *4* (1), 14–30.

(13) Haynes, C. L.; Yonzon, C. R.; Zhang, X.; Van Duyne, R. P. *J. Raman Spectrosc.* **2005**, *36* (6–7), 471–484.

(14) Halvorson, R. A.; Vikesland, P. J. *Environ. Sci. Technol.* **2010**, *44* (20), 7749–7755.

(15) Moskovits, M. In *Surface-Enhanced Raman Scattering*; Springer Berlin Heidelberg; pp 1–17.

(16) Sharma, B.; Frontiera, R. R.; Henry, A.-I.; Ringe, E.; Van Duyne, R. P. *Mater. Today* **2012**, *15* (1–2), 16–25.

(17) Le Ru, E. C.; Etchegoin, P. G. In *Principles of Surface-Enhanced Raman Spectroscopy*; Elsevier, 2009; pp 1–27.

(18) Hildebrandt, P.; Stockburger, M. *J. Phys. Chem.* **1984**, *88* (24), 5935–5944.

(19) Tian, Z.-Q.; Ren, B. *Annu. Rev. Phys. Chem.* **2004**, *55* (1), 197–229.

(20) Wu, D.-Y.; Li, J.-F.; Ren, B.; Tian, Z.-Q. *Chem. Soc. Rev.* **2008**, *37* (5), 1025.

(21) Kleinman, S. L.; Ringe, E.; Valley, N.; Wustholz, K. L.; Phillips, E.; Scheidt, K. A.; Schatz, G. C.; Van Duyne, R. P. *J. Am. Chem. Soc.* **2011**, *133* (11), 4115–4122.

(22) Zhang, R.; Zhang, Y.; Dong, Z. C.; Jiang, S.; Zhang, C.; Chen, L. G.; Zhang, L.; Liao, Y.; Aizpurua, J.; Luo, Y.; Yang, J. L.; Hou, J. G. *Nature* **2013**, *498* (7452), 82–86.

(23) Schlücker, S. *Angew. Chemie Int. Ed.* **2014**, *53* (19), 4756–4795.

(24) Craig, A. P.; Franca, A. S.; Irudayaraj, J. *Annu. Rev. Food Sci. Technol.* **2013**, *4* (1), 369–380.

(25) Zheng, J.; He, L. *Compr. Rev. Food Sci. Food Saf.* **2014**, *13* (3), 317–328.

(26) Cînta Pînzaru, S.; Pavel, I.; Leopold, N.; Kiefer, W. *J. Raman Spectrosc.* **2004**, *35* (5), 338–346.

(27) Cotton, T. M.; Kim, J.-H.; Chumanov, G. D. *J. Raman Spectrosc.* **1991**, *22* (12), 729–742.

(28) Qian, X.; Peng, X.-H.; Ansari, D. O.; Yin-Goen, Q.; Chen, G. Z.; Shin, D. M.; Yang, L.; Young, A. N.; Wang, M. D.; Nie, S. *Nat. Biotechnol.* **2008**, *26* (1), 83–90.

(29) Sharma, B.; Fernanda Cardinal, M.; Kleinman, S. L.; Greeneltch, N. G.; Frontiera, R. R.; Blaber, M. G.; Schatz, G. C.; Van Duyne, R. P. *MRS Bull.* **2013**, *38* (8), 615–624.

(30) Moskovits, M. *Rev. Mod. Phys.* **1985**, *57* (3), 783–826.

(31) Fan, M.; Andrade, G. F. S.; Brolo, A. G. *Anal. Chim. Acta* **2011**, *693* (1–2), 7–25.

(32) Wang, A.; Kong, X. *Materials (Basel).* **2015**, *8* (6), 3024–3052.

(33) Procházka, M. *Surface-Enhanced Raman Spectroscopy*; Biological and Medical Physics, Biomedical Engineering; Springer International Publishing: Cham, 2016.

(34) Swadesh, J. K. *HPLC: practical and industrial applications*; CRC Press, 2000.

(35) Anderson, D. J. *Anal. Chem.* **1999**, *71* (12), 314–327.

(36) Shintani, H. *Handbook of capillary electrophoresis applications*; Springer Science & Business Media, 2012.

(37) Grossman, P. D.; Colburn, J. C. *Capillary electrophoresis: Theory and practice*; Academic Press, 2012.

(38) Fenton, E. M.; Mascarenas, M. R.; López, G. P.; Sibbett, S. S. *ACS Appl. Mater. Interfaces* **2009**, *1* (1), 124–129.

(39) Posthuma-Trumpie, G. A.; Korf, J.; van Amerongen, A. *Anal. Bioanal. Chem.* **2009**, *393* (2), 569–582.

(40) Schrader, B. *Infrared and Raman spectroscopy: methods and applications*; John Wiley & Sons, 2008.

(41) Lewis, I. R.; Edwards, H. *Handbook of Raman spectroscopy: from the research laboratory to the process line*; CRC Press, 2001.

(42) Bantz, K. C.; Meyer, A. F.; Wittenberg, N. J.; Im, H.; Kurtuluş, Ö.; Lee, S. H.; Lindquist, N. C.; Oh, S.-H.; Haynes, C. L. *Phys. Chem. Chem. Phys.* **2011**, *13* (24), 11551.

(43) Sun, F.; Hung, H.; Sinclair, A.; Zhang, P.; Bai, T.; Galvan, D. D.; Jain, P.; Li, B.; Jiang, S.; Yu, Q. *Nat. Commun.* **2016**, *7*, 13437.

(44) Yu, W. W.; White, I. M. *Analyst* **2013**, *138* (13), 3679.

(45) Morelli, L.; Zór, K.; Jendresen, C. B.; Rindzevicius, T.; Schmidt, M. S.; Nielsen, A. T.; Boisen, A. *Anal. Chem.* **2017**, *89* (7), 3981–3987.

(46) Cheng, J.; Wang, S.; Su, X. O. *PLoS One* **2014**, *9* (9).

(47) Yu, W. W.; White, I. M. *Manuscript, Author* **2012**, *137* (5), 1168–1173.

(48) Kim, A.; Barcelo, S. J.; Williams, R. S.; Li, Z. *Anal. Chem.* **2012**, *84* (21), 9303–9309.

(49) Morelli, L.; Andreasen, S. Z.; Jendresen, C. B.; Nielsen, A. T.; Emnéus, J.; Zór, K.; Boisen, A. *Analyst* **2017**, *142* (23), 4553–4559.

(50) Lee, M.; Lee, K.; Kim, K. H.; Oh, K. W.; Choo, J. *Lab Chip* **2012**, *12* (19), 3720.

(51) Strehle, K. R.; Cialla, D.; Rösch, P.; Henkel, T.; Köhler, M.; Popp, J. *Anal. Chem.* **2007**, *79* (4), 1542–1547.

(52) Ackermann, K. R.; Henkel, T.; Popp, J. *ChemPhysChem* **2007**, *8* (18), 2665–2670.

(53) Subaihi, A.; Trivedi, D. K.; Hollywood, K. A.; Bluett, J.; Xu, Y.; Muhamadali, H.; Ellis, D. I.; Goodacre, R. *Anal. Chem.* **2017**, *89* (12), 6702–6709.

(54) Yu, W. W.; White, I. M. *Analyst* **2013**, *138* (13), 3679.

(55) Lin, M.; He, L.; Awika, J.; Yang, L.; Ledoux, D. R.; Li, H.; Mustapha, A. *J. Food Sci.* **2008**, *73* (8), T129–T134.

2 RAMAN EFFECT

Common and broadly applied optical spectroscopy techniques (e.g. Raman, Infra-red, absorption spectroscopy) are focused on analysis of light-matter interactions. The phenomenon of light scattering is one of the typical outcomes of such interactions. The information about vibrational modes of molecules, crystal orientation and other morphological parameters can be retrieved from the scattered light[1,2]. A straightforward reason for an electromagnetic (EM) wave to experience scattering, which implies change of its propagation direction, is related to optical inhomogeneity of the medium. Thus, time dependent fluctuations of local refractive index results in scattering of incident light[3]. In a general form, refractive index $\boldsymbol{n}$ of a medium is given as:

$$n^2 = 1 + M\alpha, \tag{2.1}$$

where $\boldsymbol{M}$ is concentration of molecules and $\boldsymbol{\alpha}$ is the local polarizability of the medium. According to Equation (2.1), a time-dependent change in refractive index can be originating from a varying local molecule concentration or polarizability. Particularly the last reason, fluctuations in polarizability, causes the incident EM wave to experience Raman scattering (RS) which contains information about vibrational modes of molecules in the medium.

In this chapter, one of the core element of this multidisciplinary PhD project, RS of light will be presented. In this way, physical background of the phenomena, current status, main advantages and disadvantages will be discussed. Before presenting a quantitative definition of RS using a classical approach, intermolecular oscillations and

their relationship with the polarizability will be described. To keep discussions brief, a medium containing only one sort of molecules will be considered.

2.1 Molecular Vibration Modes

In classical theory, the simplest way of defining intermolecular vibrations is "string" approximation where atoms in a molecule are assumed to interact according to Hooke's law. In addition to that, non-harmonic behavior of "string" constant $\boldsymbol{k}$ in agreement with semi-empirical models (Morse model, Lennard-Jones model) can be implemented to depict a more adequate picture of molecular systems[4]. The classical harmonic oscillator and more precise semi-empirical models cannot fully describe the interatomic interactions. These are rather complex in nature since they depend on the type of the chemical bond (ionic, metallic or covalent) and various quantum effects like

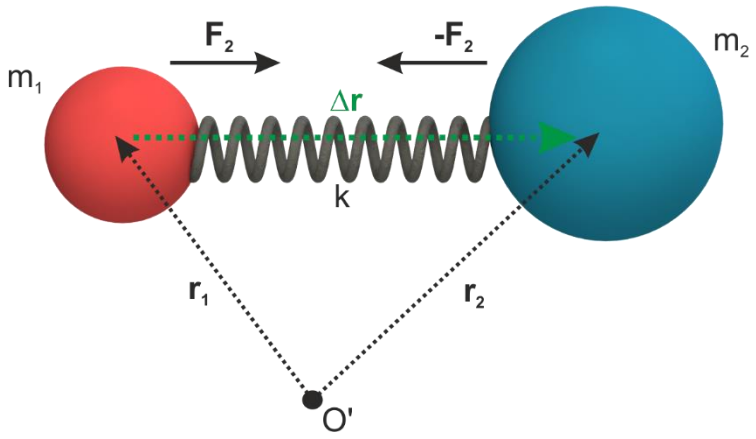

Figure 2.1 Schematic illustration of a simplified diatomic molecule. The atoms are illustrated as spheres attached through a "string" with a string constant $\boldsymbol{k}$. The spatial positions of atoms with respect to reference system $\mathbf{O'}$, relative distance between atoms and their masses are indicated through vectors $\vec{\boldsymbol{r}}_{\boldsymbol{1}}$, $\vec{\boldsymbol{r}}_{\boldsymbol{2}}$, $\boldsymbol{\Delta}\vec{\boldsymbol{r}}$, $\boldsymbol{m_1}$ and $\boldsymbol{m_2}$ respectively.

repulsion force due to Pauli exclusion principle, quantization of energy levels which cannot be represented via classical approaches[5,6].

A straightforward example of a classical model of a diatomic molecule is shown in Figure 2.1. For clarity of further derivations, only harmonic oscillations (linear force response of the "string") will be taken into account. In fact, this estimation is valid when assuming small fluctuations in non-harmonic molecular oscillations. Further, the equilibrium condition of the system will be defined at constant relative distance of $\boldsymbol{\Delta\vec{r}_0}$ between the atoms. Hence, by applying Newtons law, a differential equation of motion can be obtained:

$$m_1 \frac{d^2\vec{r}_1}{dt^2} = k(\Delta\vec{r} - \Delta\vec{r}_0), \tag{2.2}$$

$$\boldsymbol{m_2 \frac{d^2\vec{r}_2}{dt^2} = -k(\Delta\vec{r} - \Delta\vec{r}_0)} \quad , \tag{2.3}$$

$$\boldsymbol{\Delta\vec{r} = \vec{r}_2 - \vec{r}_1} \quad . \tag{2.4}$$

By combining Equation (2.2)-(2.4) the final form of the differential motion equation can be reduced to:

$$\frac{d^2(\Delta\vec{r} - \Delta\vec{r}_0)}{dt^2} = -\frac{k(m_1 + m_2)}{m_1 m_2}(\Delta\vec{r} - \Delta\vec{r}_0) \quad . \tag{2.5}$$

A general solution for the second order differential Equation (2.5), which is commonly referred in literature as equation for vibrational motion[7], can in scalar form be expressed as:

$$Q = \|\Delta\vec{r} - \Delta\vec{r}_0\| = Ae^{i\Omega t} + Be^{-i\Omega t} \quad , \tag{2.6}$$

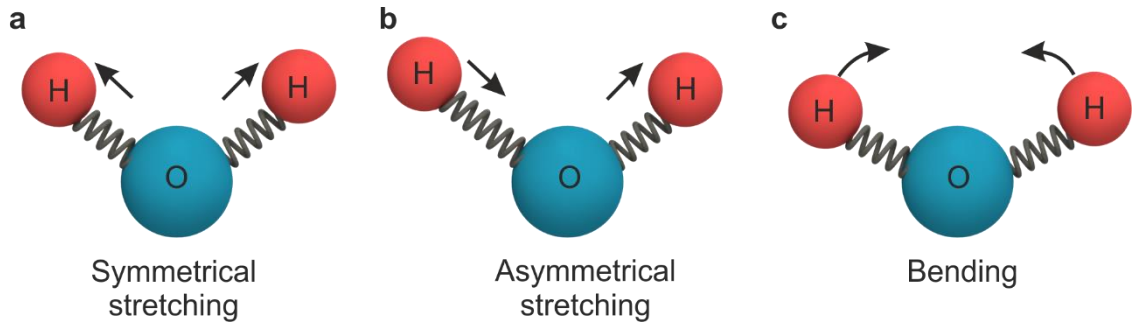

Figure 2.2 Various "normal" vibrational modes of the water molecule. The arbitrary oscillatory motion of a water molecule can be given as superposition of these three independent modes (a) symmetrical, (b) asymmetrical stretching and lastly (c) bending.

where $\boldsymbol{A}$ and $\boldsymbol{B}$ are the amplitudes and Ω is the angular frequency of vibrational motion and it is defined as:

$$\Omega^2 = \frac{k(m_1 + m_2)}{m_1 m_2} \,. \tag{2.7}$$

Now, assuming a molecule which contains $\boldsymbol{N}$ atoms, a common way to define oscillation between atoms is to utilize superposition principle. This suggests that each interatomic vibration in a molecule can be expressed in terms of independent oscillations or "normal modes" with a natural vibrational frequency $\Omega_{\boldsymbol{i}}$ (see Equation (2.7)). The total amount of modes $(3\boldsymbol{N} - 6)$ which represents degree of freedom of the molecule system is directly linked to the number of atoms in that molecule. For instance, a water molecule has 3 atoms, hence it has 3 degrees of freedom (or "normal modes"). The independent vibrational modes of a water molecule which are bending, symmetrical and asymmetrical stretching are shown in Figure 2.2. Thus, for a molecule consisting of $\boldsymbol{N}$ atoms, by

applying superposition principle, the vibration between 2 atoms can be analytically expressed in the following way:

$$Q_t = \sum_{j=1}^{3N-6} Q_j = \sum_{j=1}^{3N-6} (A_j\, e^{i\Omega_j t} + B_j e^{-i\Omega_j t}) \quad . \tag{2.8}$$

The final obtained expression for total vibration between 2 atoms, Equation (2.8), describes fully the oscillating molecule system. As a remark, the Equation (2.8) was derived by assuming harmonic interactions between atoms. Nevertheless, for upcoming subsection, this assumption is sufficient to depict the relation between polarizability of a molecular system and vibrational "normal" modes.

2.2 Polarizability of Molecules

An essential quantitative parameter describing the interaction between matter and EM waves (or light) is the polarizability of the medium. Polarizability defines the local charge distribution or more precisely the dipole moment in a unit volume (polarization) under the influence of electric field. In general terms, the molecules which form the matter can be divided into two species, (i) polar molecules which have natural dipole moment without any external impact and (ii) non-polar molecules which have negligible dipole moment[8]. An illustrative example is given in Figure 2.3a, b where polar H_2O and non-polar CO_2 molecules are shown. Thus, because of its asymmetrical charge distribution, water molecule possesses a dipole moment. Contrary, the CO_2 molecule with a linear arrangement has negligible amount of total electrical dipole moment[9]. However, taking into account the chaotic motion of polar molecules in the substances, the resulting effect of electric dipole in terms of polarization is insignificant as well.

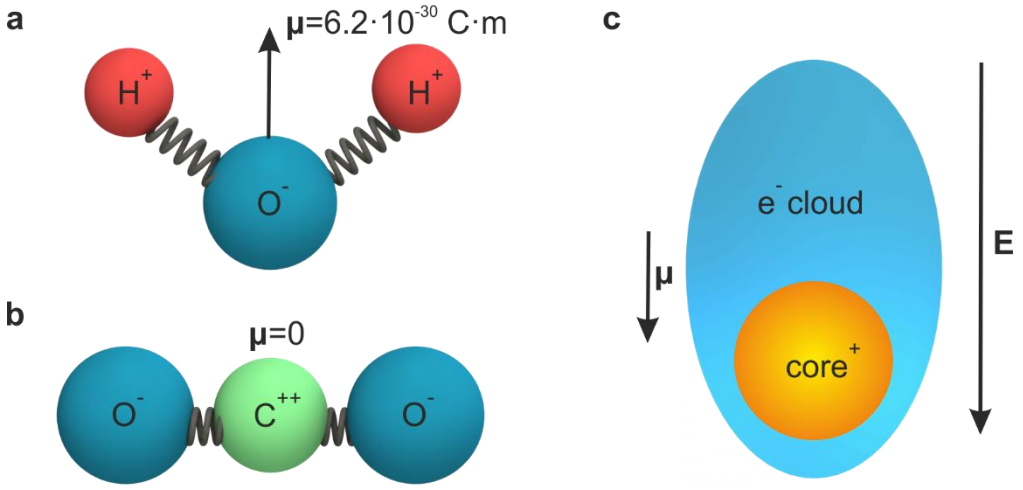

Figure 2.3 Polarizability in molecular scale. (a) Natural dipole moment of water molecule due to its linear asymmetry and charge distribution. (b) Non-polar CO_2 molecule as a result of its linear symmetry has negligible dipole moment. (c) Principle of formation of dipole moment on non-polar molecules or atoms under the effect of an electric field.

The behavior of polar and non-polar molecules under an externally applied electric field is different. For simplicity, assuming only uniformly applied fields, the molecules with naturally present dipole moment would align with respect to the field direction. In other words, the main contribution to the polarization of the substance is emerging from the dipole moments (polar molecules) which adjust their orientation with the help of Coulomb forces. On the other hand, the non-polar molecules can provide polarization of the matter as well. As it is presented in Figure 2.3c, for a neutrally charged atom, the formation of dipole moments under an external field relies on spatial shifts of localized charges. In this way, by pulling apart opposite charges, electron cloud and positively charged nuclei, the dipole moment and consequently the polarization of the

substance is achieved[8]. A similar effect will be discussed in the next chapter where the impact of EM wave on plasmonic structures is introduced. Nevertheless, regardless of the polarity of the molecule, the dipole moment has a linear correspondence with the externally applied electric field:

$$\vec{p} = \alpha \vec{E} \quad , \tag{2.9}$$

where $\vec{\boldsymbol{p}}$ is the dipole moment, $\boldsymbol{\alpha}$ is the polarizability and $\vec{\boldsymbol{E}}$ is the external electric field. One should note that the equality is valid only if the external electric field is not strong enough to result in structural changes of the molecule.

The Equation (2.9) is not precise enough in the sense that a time dependent fluctuation of the polarizability function is not defined. For most of the applications, it might be sufficient to consider the time averaged response from the electric field. But as it was stated earlier in this chapter, the RS is caused by local time dependent polarizability fluctuations of the molecule. The core understanding behind such time dependent changes in polarizability relies on the dynamic nature of molecules. More accurately, the intermolecular oscillations, which implies constantly changing distances between atoms and as a result local charge distributions suggest distinct response (polarizability) to the external field. Since the Equation (2.8) is a known time dependent function, the unknown function $\boldsymbol{\alpha}(\boldsymbol{t})$ can be decomposed around equilibrium position ($\|\boldsymbol{\Delta}\vec{\boldsymbol{r}} - \boldsymbol{\Delta}\vec{\boldsymbol{r}}_{\boldsymbol{0}}\| = 0$) using Taylor series:

$$\alpha(t) = \sum_{l=1}^{\infty} \frac{\partial^l \alpha}{\partial Q_t^l}(0) \frac{(Q_t)^l}{l!} \quad . \tag{2.10}$$

Now, assuming that the proposed Taylor series is converging, the accuracy of the model will be defined by the number of elements which would be considered. For our purpose,

first two terms are sufficient to illustrate the principle of RS. Thus, for the following expressions, the time dependent polarizability function:

$$\alpha(t) = \alpha(0) + \frac{\partial \alpha}{\partial Q_t}(0) \sum_{j=1}^{3N-6} (A_j\, e^{i\Omega_j t} + B_j e^{-i\Omega_j t}) \quad , \qquad (2.11)$$

will be used.

2.3 Rayleigh and Raman Scattering

In previous subsections, intermolecular vibrations and their relationship with the polarizability of a molecule was presented. Equation (2.9) and (2.11) provide an essential and sufficient base for classical EM interpretation of RS. The phenomenon involves an external illumination of the molecules and subsequent scattering of the light. For clarity, as an incident illumination source, monochromatic and coherent EM wave will be taken into account. The overall light scattering process is summarized in Figure 2.1Figure 2.4. As a result, the following relation can be retrieved:

$$\|\vec{p}\| = \left\|\alpha \vec{E}\right\| = \left(\alpha(0) + \frac{\partial \alpha}{\partial Q_t}(0) \sum_{j=1}^{3N-6} (A_j\, e^{i\Omega_j t} + B_j e^{-i\Omega_j t}) \right) \left(E_0 e^{i\omega_0 t}\right). \quad (2.12)$$

Hence, the final form can be reduced to:

$$\|\vec{p}(t)\| = E_0 \alpha(0) e^{i\omega_0 t} + E_0 \frac{\partial \alpha}{\partial Q_t}(0) \sum_{j=1}^{3N-6} (A_j\, e^{it(\omega_0 + \Omega_j)} + B_j e^{it(\omega_0 - \Omega_j)}), \quad (2.13)$$

where $\boldsymbol{E_0}$ is the electric field amplitude and $\boldsymbol{\omega_0}$ is the angular frequency of the incident EM wave. It's a well-known fact that an oscillating electric dipole $\vec{\boldsymbol{p}}(\boldsymbol{t})$ acts as a source of light. Moreover, the oscillation frequency of the dipole is directly linked to the

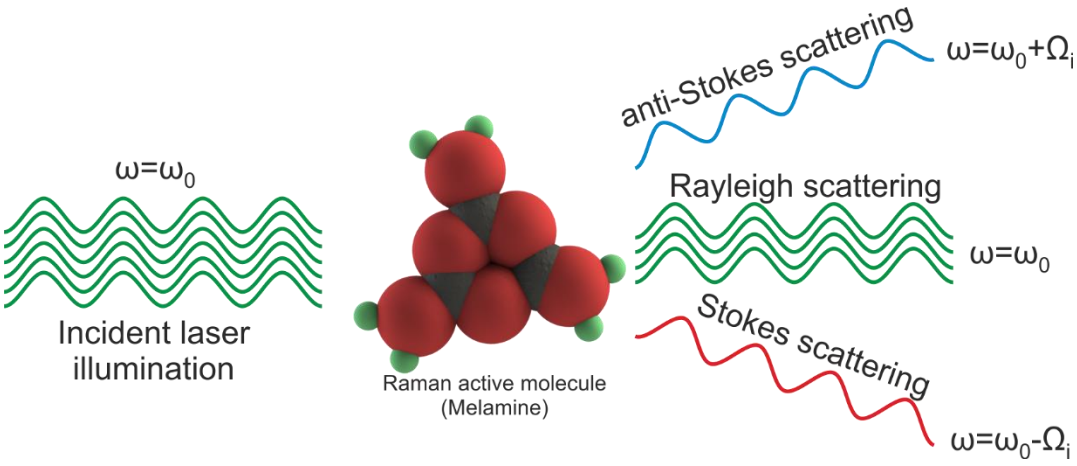

Figure 2.4 Schematic illustration of the scattering process. As a result of illumination of a Raman active molecule (melamine) with incident EM wave with angular frequency of $\boldsymbol{\omega_0}$, three distinct types of scattering processes take place. Those are Rayleigh, Stokes and anti-Stokes scattering of the light.

frequency of the emitted light and in a similar manner, the amplitude of dipole oscillation defines the power of the total emitted light. In such manner, the first term of Equation (2.13) represents the Rayleigh scattering of the incident light where the scattered light has exactly the same angular frequency as compared to the incident EM wave. Further, the last term of the equation represents the inelastic RS of the light with divergent angular frequency of the dipole oscillation. Commonly in literature, the oscillation with higher frequency $\boldsymbol{\omega_0} + \Omega_j$ is referred to as anti-Stokes scattering while the lower frequency $\boldsymbol{\omega_0} - \Omega_j$ is Stokes scattering of incident light. It is evident that both Stokes and anti-Stokes scattering of the light contains spectroscopically rich information about the vibrational modes of the molecule. However, the RS of light relies on certain conditions. First of all, the intensity of Rayleigh scattering dominates over RS and it's a typical event for all sort of molecules. This can be correlated with the fact that all types of molecules

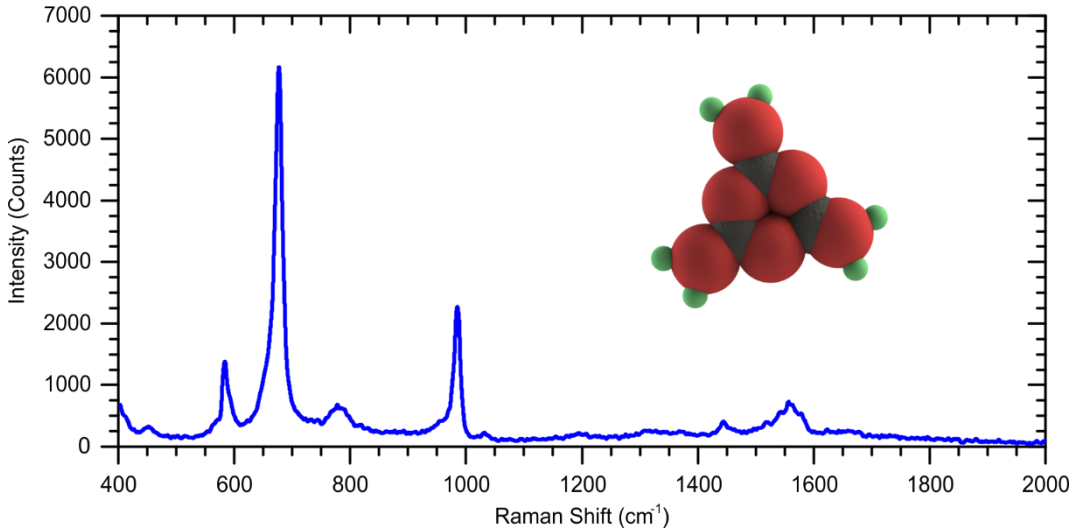

Figure 2.5 Raman spectrum of melamine recorded at 785 nm laser illumination.

can be polarized to some extent. On the other hand, less probable event RS (only 10^{-5} part of incident light) requires non-zero polarizability gradient (around the equilibrium position) with respect to intermolecular vibrations[10]:

$$\frac{\partial \alpha}{\partial Q_t}(0) \neq 0 \quad . \tag{2.14}$$

If the specification (selection rule) in Equation (2.14) is fulfilled, the molecule is called Raman active. As an example, a spectrum of the Raman active molecule melamine recorded at 785 nm laser illumination is shown in Figure 2.5. Here, Stokes scattering on melamine crystal structures (intensity) and accordingly the intermolecular vibration modes are presented through Raman shift which gives relative deviation from the laser wavelength ($\boldsymbol{\lambda_{laser}}$) in terms of wavenumbers:

$$Raman\ shift = \left(\frac{1}{\lambda_{laser}} - \frac{1}{\lambda_1}\right) \quad , \tag{2.15}$$

where $\boldsymbol{\lambda_1}$ is the wavelength at which scattering intensity is measured.

As it was mentioned previously in this chapter, the classical approach is not adequate to give a full picture of the RS phenomenon. The classical approach turns out to be sufficient to predict Rayleigh scattering accurately. However, the classical model (Equation (2.13)) is adequate only for qualitative definition of RS, which means that it can be utilized to determine the frequency of the scattered EM wave. Further, the classical assumption of RS intensity, in other words quantitative evaluation of the process is valid only for limited cases. Moreover, Equation (2.13) describes only the vibrational RS neglecting the rotational modes. The pure origin of those problems lies on various mechanisms such as restriction rules for quantized energy level transitions, population of energy states and discretization of rotational modes which are not present in classical approach[10].

2.4 Raman Spectroscopy

Nowadays, Raman spectroscopy is a widely employed technique. Commonly, the spectroscopic tool is utilized for sample analysis in various applications of biomedical, environmental, pharmaceutical and semi-conductor research fields. The technique enables one to identify and at the same time quantify certain analytes using the fingerprint spectra in a broad range specimens (liquids, solids and gasses) which makes the Raman spectroscopy a highly specific and versatile tool. Moreover, the method does not require expertise in sample preparation and it is also possible to acquire spectral response within seconds from very small sample amounts (for liquids ~µl). According to recent studies, ~µM detection limit of analyte molecules with high Raman cross-section

is possible to achieve[9,10]. Nevertheless, for some application cases, the technique is incapable of performing a sample analysis. The main disadvantages of Raman spectroscopy can be addressed to the nature of light matter interactions. First of all, along with the scattering process, the incident light can also excite electronic states of molecules in specimen which eventually would result in fluorescence emission. Taking into account that the RS effect is weak (only 10^{-5} part of incident light), the broad fluorescence background signal would cover the spectroscopic fingerprints of the molecule. For example, a broad fluorescence background signal is observed in Raman measurements of alkaloids on plant cell samples using an excitation wavelength of 365 nm. Even though the analyte molecule is not fluorescent under 365 nm excitation wavelength, because of the chemically rich environment of the biological sample, fluorescent background signal from macromolecules are prohibiting the analysis of the analyte molecule[12]. One way to overcome this issue is to utilize different excitation laser sources for example in near infra-red region. However, the Raman scattering intensity ($\boldsymbol{I_{Raman}}$) is highly dependent on excitation wavelength ($\boldsymbol{\lambda_{Laser}}$)[13]:

$$I_{Raman} = \frac{I_{Laser}}{\lambda_{Laser}^4} \quad , \tag{2.16}$$

where $\boldsymbol{I_{Laser}}$ is the intensity of incident laser. Optionally this can be compensated by increasing the excitation laser intensity. Unfortunately, in most cases, this leads to destructive effects on the molecular structure of analytes through local heating of the laser.

References

(1) Chylek, P.; Ramaswamy, V.; Ashkin, A.; Dziedzic, J. M. *Appl. Opt.* **1983**, *22* (15), 2302.

(2) Pecora, R. *Dynamic light scattering: applications of photon correlation spectroscopy*; Springer Science & Business Media, 2013.

(3) Stockmayer, W. H. *J. Chem. Phys.* **1950**, *18* (1), 58–61.

(4) John R. Ferraro, Kazuo Nakamoto, C. W. B. *Introductory Raman spectroscopy*; Boston : Academic Press, 2003.

(5) Brown, J. M.; Carrington, A. *Rotational spectroscopy of diatomic molecules*; Cambridge University Press, 2003.

(6) Hollas, J. M. *Modern spectroscopy*; John Wiley & Sons, 2004.

(7) Thomson, W. *Theory of vibration with applications*; CRC Press, 1996.

(8) Griffiths, D. J. *Introduction to Electrodynamics*; Prentice Hall, 1999.

(9) Nir, S.; Adams, S.; Rein, R. *J. Chem. Phys.* **1973**, *59* (6), 3341–3355.

(10) Long, D. A. *The Raman Effect*; John Wiley & Sons, Ltd: Chichester, UK, 2002.

(11) Schrader, B. *Infrared and Raman spectroscopy: methods and applications*; John Wiley & Sons, 2008.

(12) Petry, R.; Schmitt, M.; Popp, J. *ChemPhysChem* **2003**, *4* (1), 14–30.

(13) Cox, A. J.; DeWeerd, A. J.; Linden, J. *Am. J. Phys.* **2002**, *70* (6), 620–625.

3 SURFACE-ENHANCED RAMAN SCATTERING

In Chapter 1 classical depiction of RS phenomenon and a brief overview of the spectroscopic tool which is based on this effect was given. As it was mentioned, the capability of Raman spectroscopy to record fingerprint spectrum of molecules in the specimen and in this way distinguishing them among each other has attracted a great interest for various practical implementations. For instance, Raman spectroscopy is a suitable tool for electrochemistry (EC) applications to monitor the surface reactions on conductive electrodes. However, in some cases, the detection limit which the Raman technique can provide is not sufficient for detecting the molecular absorption events on electrode surfaces. One way to overcome this is to utilize porous electrode structures with higher surface area. Thus, during the EC treatment of the sample, the surface concentration of distinct absorbed molecules on the electrode ($\boldsymbol{M}$) would be increased[1]. It is obvious that the Raman signal for a specific molecule type is linearly dependent on number of excited molecules or more precisely the amount of Raman scatterers in the laser spot. Using the Equation (2.13), in a simple manner, the Raman scattering intensity can be given in the following way:

$$I_{Raman} \sim M \ \left\|\vec{E}_0\right\|^2 \left(\frac{\partial \alpha}{\partial Q_t}\right)^2 \quad , \tag{3.1}$$

where $\left\|\vec{\boldsymbol{E}}_{\boldsymbol{0}}\right\|^{\boldsymbol{2}}$ is related to intensity of the laser illumination and $\left(\frac{\boldsymbol{\partial \alpha}}{\boldsymbol{\partial Q_t}}\right)$ is associated with the Raman activity (cross-section) of the molecule. A similar study was carried out by

Fleischmann et al., where roughened Ag electrodes were employed for EC measurements of pyridine molecules[2]. According to their observations, enormous boost of Raman signal from pyridine molecules on electrode surface was not correlated with the increased surface area. This was the first experimental report on the surface-enhanced RS effect on roughened Ag surface which suggested a unique boosting mechanism. Over the past decades, multiple theoretical and experimental investigations on understanding the working principle of this surface phenomenon on different roughened metal surfaces were conducted[3–5]. As a result, the boost of RS is explained in terms of two contributing fundamental principles. First, the EM enhancement mechanism which results in a local increase of the electric field, $\left\|\vec{\boldsymbol{E}}_{\boldsymbol{0}}\right\|^{\boldsymbol{2}}$ term in Equation (3.1). Further, a chemical enhancement mechanism which occurs due to electron band interaction between the analyzed molecule and the metal surface (e.g. Ag), $\left(\frac{\boldsymbol{\partial \alpha}}{\boldsymbol{\partial Q_t}}\right)$ term in Equation (3.1). Particularly the last mechanism indicates that the analyzed molecule and the metal surface cannot be treated as two isolated systems. Instead, the bound system should be characterized as one individual system with unique polarizability and Raman cross-section. In fact, this mechanism is significantly dependent on the molecule and the interacting metal type[6]. However, for the broad variety of roughened conducting surfaces, the main contribution for enhancement is achieved through the EM mechanism[7]. For this reason, in upcoming sections, the basic concepts of surface-enhanced RS phenomenon in terms of EM boosting principle will be presented.

3.1 EM Waves in Conducting Environment

It should be noted that in consonance with the experimental observations, the surface-enhanced RS phenomenon was observed on roughened surfaces (in most of the cases nanostructured) of conducting noble metals such as Ag, Au, Al and Cu[7]. Therefore,

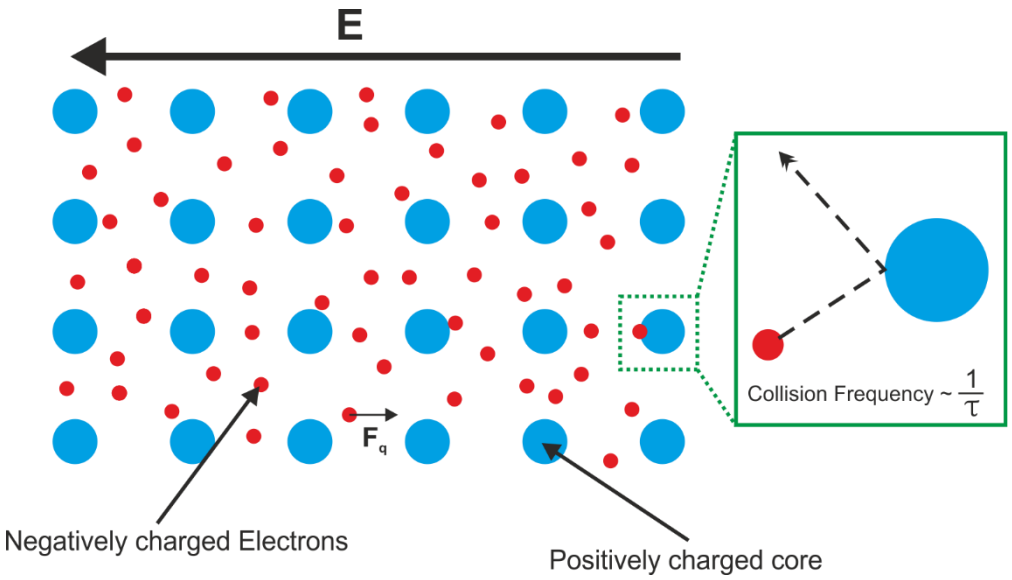

Figure 3.1 Drude model for electron transfer in conducting materials. The positively charged metal ions are illustrated as blue spheres and the charge carriers (electrons) of the conductor is presented as red spheres. The charge transfer which proposes net collective motion of electrons is facilitated by an externally applied electric field ***E***. Further, the dissipative interaction between electrons and ions is characterized through a characteristic collision frequency parameter.

before giving a theoretical explanation on EM enhancement mechanism, the behavior of the conductive materials under the impact of external EM wave should be described. As it was pointed out in Section 2.2, the response of matter under an electric field is characterized in terms of molecular polarizability when dealing with microscale systems. However, the dielectric permittivity function, which defines the polarization (dipole moment in unit volume) is more suitable for interpretation of macroscale systems like roughened Ag surface. It should be emphasized that the dielectric function was initially introduced to define insulators that have limited capacity for charge transfer. Moreover, under a static electric field, the polarization would be linearly dependent on the amplitude

of the field. Indeed, under the effect of static electric field, the dielectric permittivity is not applicable for conductor materials due to presence of the unbound electrons. Nevertheless, the dielectric permittivity function can be associated with if the applied field is oscillating (EM wave). Under this circumstance, the spatial migration of charge carriers in conductors would be restricted due to time dependent changes in the electric field direction[8].

Generally, a conductive material can be classified as a system of atoms which consists of unbound or more specifically "loose electrons" which are easily distorted under any external EM influence. In this way, the conductivity of e.g. metals is explained as a flow of electrons which are easily brought into motion by means of an applied electric field[8]. In the early 1900's the theoretical investigation of charge transport in conductive materials attracted great interest. The simplest and also accurate classical representation of electron motion in metals under an external perturbation can be achieved through the Drude model (Figure 3.1). Thus, according to the model, the conductor is assumed to be arrangement of positively charged metal ions, which are firmly positioned in a periodic configuration and a uniformly distributed mobile electron cloud. Additionally, the chaotic nature of electron motion is described via a characteristic parameter of a material, the relaxation time. In summary, the relaxation time defines statistically averaged collision frequency ($\boldsymbol{\varphi}$) between an electron in motion and immobile positively charged ions in the metal. It is obvious that the relaxation time would be defined by multiple factors like density, charge and mass of the ions and electrons in the metal[8–10]. Taking into account all the aspects, the equation of motion for an electron under EM wave, according to Drude model can be expressed as:

$$m_e \frac{d^2\vec{r}}{dt^2} = -q\vec{E}_0 e^{i\omega t} - m\varphi \frac{d\vec{r}}{dt} \quad , \tag{3.2}$$

where $\boldsymbol{m_e}$ and $\boldsymbol{q}$ are the mass and the absolute charge of the electron, and $\vec{\boldsymbol{E}}_{\boldsymbol{0}}$ defines the amplitude of EM wave with angular frequency of $\boldsymbol{\omega}$. The second order differential Equation (3.2), has a following general solution[10]:

$$\|\vec{r}(t)\| = \frac{q\|\vec{E}_0\|e^{i\omega_0 t}}{m(\omega^2 + i\varphi\omega)} \quad . \tag{3.3}$$

Here, the imaginary part of the solution describes the phase shift of electron's oscillation with respect to the incident wave. It is apparent that, if the dissipative forces or in other words the collision frequency is higher, the electron would have a delayed response (damping) which is represented by the imaginary part in Equation (3.3). Next, to obtain the polarization in the conductor generated by means of an external field, the total contribution of electrons in the Drude model must be included. In this way, assuming that the density of electrons is $\boldsymbol{n}$, the scalar form of polarization $\|\vec{\boldsymbol{P}}(\boldsymbol{t})\|$ induced by spatial displacement $\|\vec{\boldsymbol{r}}(\boldsymbol{t})\|$ will be:

$$\|\vec{P}(t)\| = -nq\|\vec{r}(t)\| = \frac{-nq^2}{m(\omega^2 + i\varphi\omega)}\ \|\vec{E}_0\|e^{i\omega t} \quad . \tag{3.4}$$

Moreover, using the definition of electric displacement $\|\vec{\boldsymbol{D}}(\boldsymbol{t})\|$:

$$\|\vec{D}(t)\| = \varepsilon\|\vec{E}_0\|e^{i\omega t} = \varepsilon_0\|\vec{E}_0\|e^{i\omega t} + \|\vec{P}(t)\| \ , \tag{3.5}$$

the relative dielectric permittivity function (dispersion relation) of the conductor material $\boldsymbol{\varepsilon_r(\omega)}$ can be retrieved:

$$\varepsilon_r(\omega) = \ 1 - \frac{\frac{nq^2}{\varepsilon_0 m}}{\omega^2 + i\varphi\omega} = 1 - \frac{\omega_p}{\omega^2 + i\varphi\omega} \ , \tag{3.6}$$

where $\boldsymbol{\varepsilon_0}$ is the permittivity of free space and $\boldsymbol{\omega_p} = \frac{\boldsymbol{nq^2}}{\boldsymbol{\varepsilon_0 m}}$ is the plasma frequency[10] of electron cloud.

It should be highlighted that the final form of Equation (3.6) was acquired using the Drude model of free electron gas. Considering the electronic bands of noble metals, the Drude model requires some extensions in order to depict a more realistic behavior of charge carriers. First of all, the internal polarization caused by positively charged metal ions can be represented by a new dielectric constant $\boldsymbol{\varepsilon_\infty}$ instead of free space permittivity. Additionally, the effect of electronic interband transitions can be classically interpreted by including the internal bound electrons[11]. Thus, the second order differential equation in this case would be:

$$m_e \frac{d^2\vec{r}}{dt^2} = -q\vec{E}_0 e^{i\omega t} - m\varphi \frac{d\vec{r}}{dt} - m\omega_0^2 \vec{r} \quad , \tag{3.7}$$

where the $\boldsymbol{\omega_0}$ term suggest angular frequency at which the interband transition occurs. However, the final form of Equation (3.6) would be sufficient to have an illustrative depiction of noble metal's behavior under the impact of external EM wave.

3.2 Scattering on Spherical Particles

Now, having the classical interpretation and a quantitative model which describes the behavior of noble metals under the act of external EM field, an idealized example system can be used to illustrate the basic principle of the EM boosting mechanism. Along with that, one of the fundamental excitation principle in plasmonics, localized surface plasmons (LSP) will be introduced. Also, it will be shown that under specific circumstances at the dielectric interface, a resonance condition and consequently significantly higher EM field enhancement can be achieved. These core elements will be

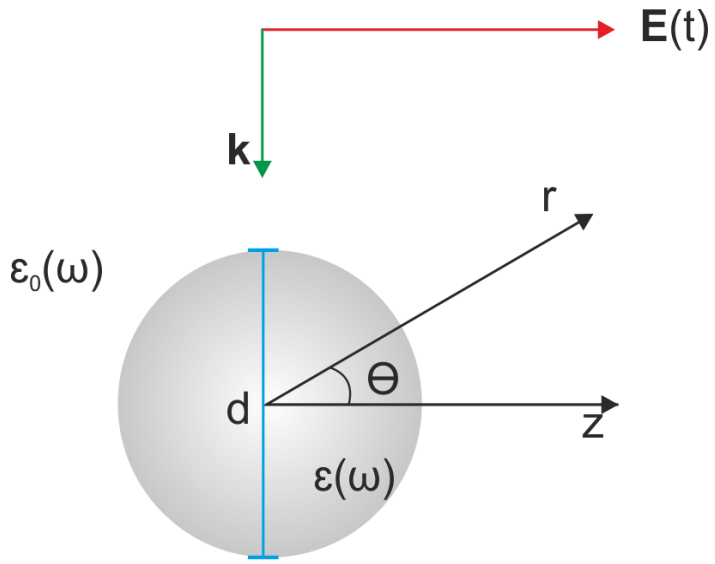

Figure 3.2 The schematics of general Mie problem. In the Mie model, illumination and as a result scattering on a spherical particle with diameter $\boldsymbol{d}$ and dielectric permittivity $\boldsymbol{\varepsilon(\omega)}$ placed in non-absorbing environment (e.g. vacuum $\boldsymbol{\varepsilon_0}$) is studied. Due to spherical symmetry, an analytical solution of the Mie scattering problem can be obtained.

demonstrated using the quasi-static Mie model, the interaction of homogeneous spherical particle with the external EM wave. In this way, the roughened electrode surface which was referred in the introductory part of this chapter will be assumed to be spherical particle or more precisely an arrangement of spherical particles[12,13]. Moreover, the quasi-static approximation requires the diameter of spherical metallic particle to be negligible as compared to wavelength of the EM radiation ($\boldsymbol{\lambda \gg d}$)[10]. The electrodynamic Mie problem is greatly simplified by quasi-static approach which allows to employ electrostatic assumption for the model. Moreover, cylindrical coordinate system will be utilized in order to provide clarity in the following discussions and analytical formulations.

The graphical representation of Mie scattering problem on a spherical particle is shown in Figure 3.2. Due to the assumption $\boldsymbol{\lambda} \gg \boldsymbol{d}$, the electrodynamic problem is reduced to the electrostatic Laplace equation which can be used to retrieve the electric potential ($\boldsymbol{V}$) values at a given spatial position $\boldsymbol{r}$. In other words, the electric field component of EM wave ($\boldsymbol{E_0 \hat{z} e^{i(\omega t + \vec{k}\cdot\vec{r})}}$) with small wavenumber $\vec{\boldsymbol{k}}$ would imply slowly developing field oscillation on a spherical particle. Thus, since the electric field stimulation can be considered to be uniform on the particle, at a given time the electrostatic condition of the system would be characterized using the following equation:

$$\nabla^2 V = 0 \quad , \tag{3.8}$$

and correspondingly the electric field at a given point will be:

$$\vec{E} = -\vec{\nabla} V \quad . \tag{3.9}$$

The general solution of differential Equation (3.8) is[14]:

$$V(r,\theta) = \sum_{l=0}^{\infty} (A_l r^l + B_l r^{-(l+1)}) P_l(cos\theta) \quad , \tag{3.10}$$

Where the $\boldsymbol{P_l(cos\theta)}$ term is the $\boldsymbol{l}$'th order Legendre Polynomials and $\boldsymbol{A_l}$, $\boldsymbol{B_l}$ are the constants which can be determined from the boundary conditions. In order to obtain the boundary conditions and subsequently the potential values inside $\boldsymbol{V_{in}}$ and outside $\boldsymbol{V_{out}}$ of the scattering object, a specific phase of time dependent EM field should be considered. In this particular case, a stage where the electric field component is maximum ($\boldsymbol{E_0}$) will be taken into account. In such manner, using the Gauss law, two boundary conditions for electric displacement at the surface of particle $\boldsymbol{r = \frac{d}{2}}$ and electric field at $\boldsymbol{r \to \infty}$ can be formulated in the following way[15]:

$$-\varepsilon\, \vec{\nabla}\, V_{in}\big|_{r=\frac{d}{2}} = -\varepsilon_0\, \vec{\nabla}\, V_{out}\big|_{r=\frac{d}{2}} \quad , \tag{3.11}$$

$$-\vec{\boldsymbol{\nabla}}\, \boldsymbol{V_{in}}\big|_{\boldsymbol{r\to\infty}} = -\,\vec{\boldsymbol{\nabla}}\, \boldsymbol{V_{out}}\big|_{\boldsymbol{r\to\infty}} \quad . \tag{3.12}$$

By applying the boundary conditions Equation (3.11) and (3.12), the potential values inside and outside the spherical scattering particle according to Equation (3.10) will be:

$$V_{in} = -\frac{3\varepsilon_0}{\varepsilon + 2\varepsilon_0}\, E_0 r\, cos\theta \quad , \tag{3.13}$$

$$\boldsymbol{V_{out} = -E_0 r\, cos\theta + E_0 \left(\frac{d}{2}\right)^3 \frac{cos\theta}{r^2}\, \frac{\varepsilon - \varepsilon_0}{\varepsilon + 2\varepsilon_0}} \quad . \tag{3.14}$$

The last term of Equation (3.14) can interpreted as spatial electric potential distribution of a point dipole source[10]. Since the constrain for the quasi-static approximation is based on $\boldsymbol{\lambda \gg d}$ condition, the interaction between EM wave and the spherical particle is occurring in a rather uniform way. More precisely, taking into consideration the $\boldsymbol{\lambda \approx d}$ condition, the influence of field components on the scattering object would not be even due to the spatial phase differences of the propagating EM wave. Likewise, in the quasi-static approximation the phase variance is negligible when compared to the dimensions of the particle. The particle can thus be treated as a point dipole source.

3.3 Localized Surface Plasmons

Despite of the fact that the proposed Mie model is neglecting the accurate nature of light-spherical particle interaction, Equation (3.14) depicts to some extend the dependence of spatial electric field distribution on geometrical parameter (diameter) and optical properties of noble metals. The precision of the analytical approach can be

expanded by introducing further adjustments. For instance, using modified long wavelength approximation (MLWA)[16] in the Mie model, analytical solutions with better correlation as compared to experimental observation can be achieved[17]. Additionally, the Drude approach, which describes the optical properties (dielectric permittivity function) Equation (3.6) of conducting materials can be exploited in the Mie model to demonstrate the behavior of spherical noble metal particles under the impact of EM wave. Prior to that, it should be noted that the distinct solutions obtained from the quasi-static Mie model is corresponding to one particular phase of EM oscillation. Hence, to get the full picture of light-metallic sphere interaction, a time dependent study of the Mie system should be conducted. In this way, considering only the quasi-static model, the linear field dependence in Equation (3.13) and (3.14) is indicating that the particle can be treated as an oscillating point dipole under the effect of propagating EM wave. This time dependent action is demonstrated in Figure 3.3.

The physical explanation of such time dependent variation in polarization of the spherical conducting particle under the impact of EM field (Figure 3.3) is accounted for spatial shifts of local unbound electrons. Thus, the phenomenon which proposes oscillatory motion of local charge carriers in sub-wavelength conducting objects facilitated by means of EM perturbation is in literature referred to as LSP excitation[10,18]. Further, from the Drude representation of conductors Equation (3.6), it is evident that the response of a conducting material is dependent on the wavelength of incident EM radiation (from the dispersion relation). Hence, for a particular plasmonic material (e.g. Ag), the wavelength of external illumination would influence the degree of LSP excitation and as a consequence the amplitude of the dipole oscillation. This is originating from the fact that, any kind of oscillatory system (e.g. Drude model) implies a natural mode (resonance frequency) at which the energy transfer from the source (EM radiation) to the system (electron cloud motion) is maximized[19]. Moreover, one of the significant

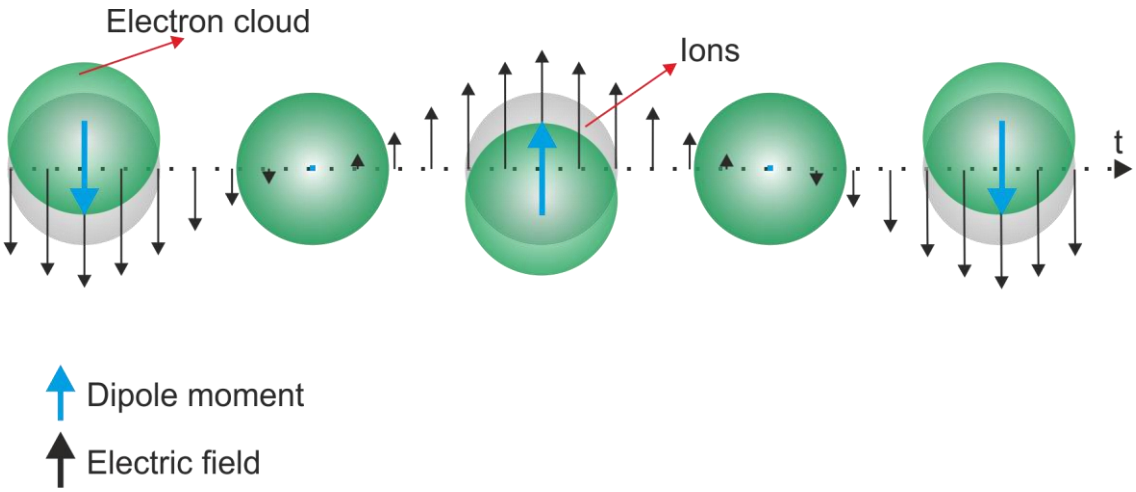

Figure 3.3 Electron cloud oscillation in spherical particles under the impact of external EM wave. The unbound electron cloud and positively charged ions of spherical metallic particle are illustrated using green and grey colors respectively. Here, time dependent shift of electron clouds under the effect of propagating EM wave and as a result polarization of the particle are schematically represented.

outcomes of the LSP excitation is the light scattering phenomenon which occurs through oscillatory motion of "dipole" source (Rayleigh scattering). In fact, the dipole radiation is angle dependent and it implies that the radiated light would have preserved wavelength compared to the incident illumination. In the following, LSP resonance and resulting boosting of the near-field EM radiation on plasmonic particles will be presented. One should consider that the analytical Mie model is only suitable for the spherical particles. On top of that, even considering the spherical materials, the analytical approach is not suitable for studying arrangement of interacting particles. Alternatively, additional computational methods e.g. finite-difference time-domain (FDTD) technique can be utilized to imitate the field response of a conducting material with a custom morphology

(e.g. spherical dimer structures). Briefly, the FDTD method employs the discretized form of the electrodynamic Maxwell equations[20]:

$$\vec{\nabla} \cdot \vec{D} = \rho_f \quad , \tag{3.15}$$

$$\vec{\boldsymbol{\nabla}} \cdot \vec{\boldsymbol{B}} = \mathbf{0} \quad , \tag{3.16}$$

$$\vec{\boldsymbol{\nabla}} \times \vec{\boldsymbol{E}} = -\frac{\boldsymbol{\partial}\vec{\boldsymbol{B}}}{\boldsymbol{\partial t}} \quad , \tag{3.17}$$

$$\vec{\boldsymbol{\nabla}} \times \vec{\boldsymbol{H}} = \vec{\boldsymbol{J_f}} + \frac{\boldsymbol{\partial}\vec{\boldsymbol{D}}}{\boldsymbol{\partial t}} \quad , \tag{3.18}$$

to presume time dependent response of the simulated environment. Here, $\vec{\boldsymbol{D}}$ stands for electric displacement, $\boldsymbol{\rho_f}$ unbound free charge density, $\vec{\boldsymbol{B}}$ magnetic field, $\vec{\boldsymbol{H}}$ auxiliary magnetic field and $\vec{\boldsymbol{J_f}}$ free current density respectively.

The degree of LSP excitation, scattering cross-section for spherical Au dimer structures calculated through FDTD computational method, is depicted in Figure 3.4. The resonance condition can be clearly visualized in Figure 3.4c, d where a peak in scattering cross-section or maximized energy transfer between incident illumination and the plasmonic particles is achieved at ~530 nm. Alternatively, the case shown in Figure 3.4a, b, proposes LSP resonance peak shifts with changing gap sizes. Here, another practical use of computational methods for LSP applications is demonstrated. Unlike the Mie model where the analytical model is achieved through tedious derivations (Equations (3.13) and (3.14)), FDTD modelling provides opportunity to imitate the interaction between distant plasmonic objects. In this case, the electron cloud oscillation in both of the spherical Au particles throughout the EM wave perturbation process are

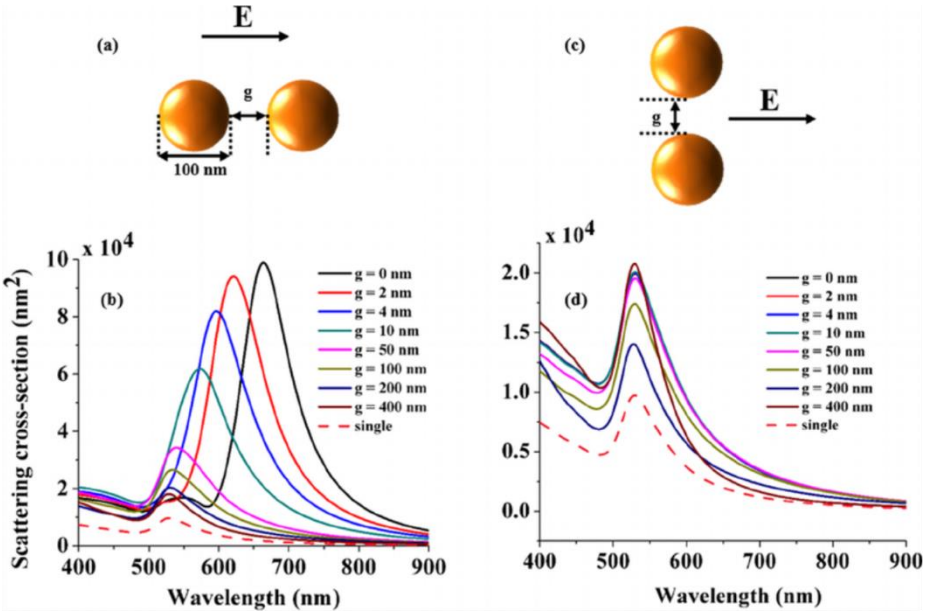

Figure 3.4 Scattering cross-section of spherical dimer structures with different gap distances. (a, b) Gab distance dependent cross-section calculations of spherical dimer structures. The electric field direction of incident illumination (polarization) is towards the dimer orientation. (c, d) Similarly, the calculated scattering cross- section of dimer s with perpendicular arrangement. Adapted from reference[23].

electrostatically influencing ("dipole-dipole" interaction) each other. As a consequence, the natural LSP mode of the spherical Au particles is shifted[21].

Another essential point for understanding the EM boosting mechanism of surface-enhanced RS is related to the near-field scattering phenomenon of LSP excitation. A typical illustration for the localized scattering intensity at the LSP resonance condition is shown in Figure 3.5. Here, the spatial distribution of the second power of the relative electric field (with respect to incident field) or the relative scattering intensity for 10 nm dimer gap size and geometrical condition summarized in Figure 3.4a is presented. The resonance condition from Figure 3.4b suggest incident illumination at 563 nm wavelength

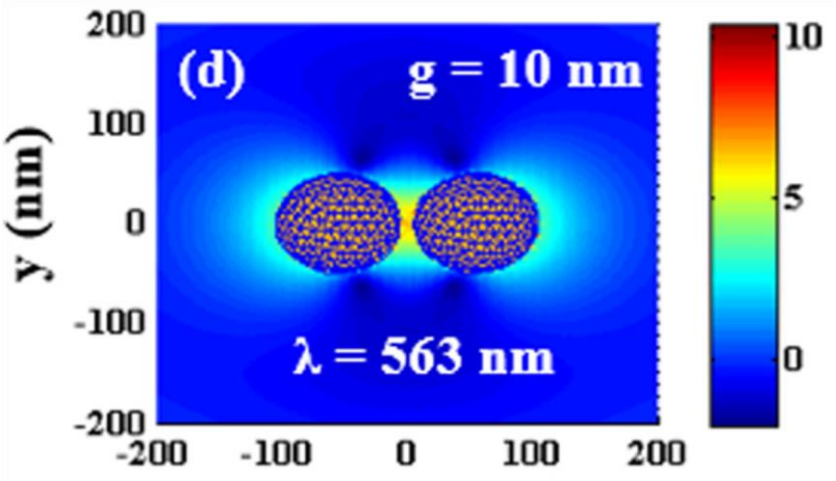

Figure 3.5 LSP excitation and scattering on the spherical Au dimer structures. The incident EM illumination with 563 nm wavelength (resonance condition) results in LSP excitation in spherical dimer structures. Subsequently, the induced scattering effect is summarized in terms of spatial square of the relative electric field (intensity) arrangement in logarithmic scale. Adapted from reference[23].

at which the FDTD simulations in Figure 3.5 were performed. Further, from Figure 3.5, the "hot-spots" or the spot with highest scattering intensities can be easily determined. A parallel depiction can be made with optical lenses which enables the incident light beam to be focused in a comparably narrow spot. Similarly, the plasmonic particles, in this case Au dimer spheres are focusing the incident coherent and monochromatic beam in nanoscale "hot-spots". It is obvious that, depending on the morphology of the plasmonic material and in broader sense, the arrangement of multiple plasmonic particles, determines the LSP modes and consequently the localized scattering intensities. In this way, plasmonic engineering of subwavelength conducting particles can be utilized for manipulation of incident radiation in nanoscale dimensions.

3.4 EM Enhancement Mechanism

The enhancement phenomenon of RS is related to near-field properties of plasmonic noble metal surfaces under influence of external illumination. For the case with spherical dimer structures, it was shown in Figure 3.5 that the field response close to the surface (especially at the gap) is substantially increased. Assuming a Raman active molecule placed in this EM "hot-spot", an evident enhancement of RS due to localized intensity of exciting illumination can be interpreted (see Equation (3.1) for RS intensity). Indeed, to get a full picture of the system, the electro-dynamic system of plasmonic surface and the molecule of interest (Raman probe) should be studied. The RS boosting mechanism which is a two-step process, is dependent on synergistic EM interaction of a plasmonic rough surface and molecule system with the incident radiation[22]. The electron band interaction between the surface of the noble metal and the Raman active analyte can give rise to another boosting mechanism (chemical enhancement). Because, the chemical boosting mechanism is highly dependent on the type of molecule and the interacting plasmonic material, the effect will be neglected. Moreover, as reported in various studies, in most of the cases the main contribution to the enhancement factor (EF) is accounted for by the EM mechanism. Typically, chemical EF is ranging from 10 to 10^2 while the EM mechanism can yield EF up to 10^8 (depending on morphological and material properties)[7].

In Figure 3.6, the general concept of a two-step EM enhancement mechanism of RS on plasmonic surfaces is presented. The first contributing boosting mechanism is obtained through LSP excitation of metallic particles. For simplicity, a spherical metal dimer structures will be given as an example. In Section 3.3, the localized enhancement (as compared to incident radiation, see Figure 3.5) of EM field as a result of LSP excitation was given. The LSP excitation and the following scattering effect occurs in

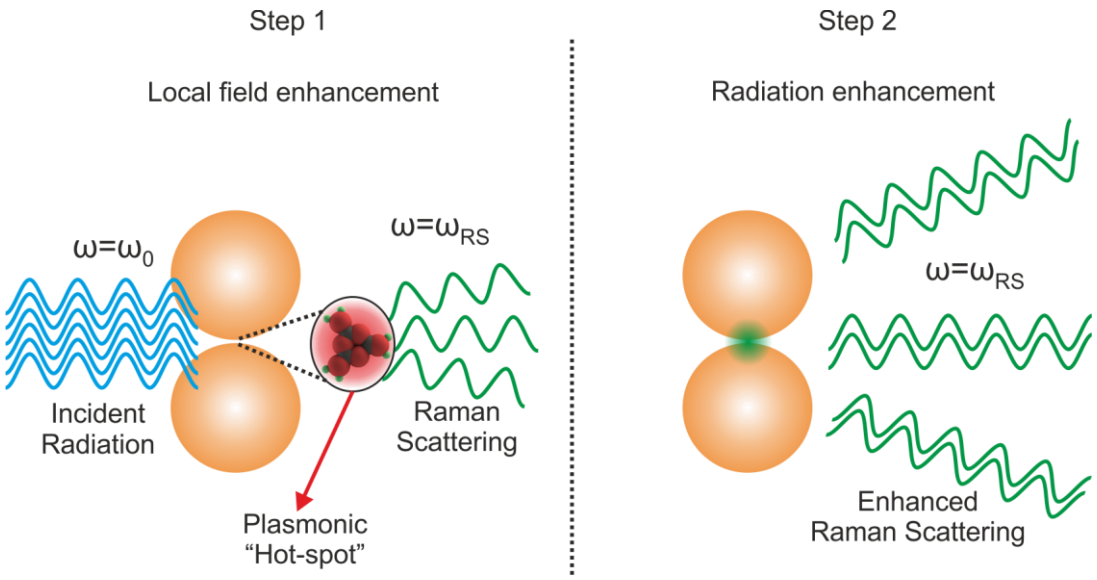

Figure 3.6 Two-step EM enhancement mechanism of RS. The first stage of EM boosting principle is achieved through near-field intensification of incident radiation with angular frequency $\boldsymbol{\omega_0}$ on the surface of plasmonic material. Further, the Raman active molecule located in the plasmonic "hot-spot" would generate enhanced RS effect. Lastly, the second step proposes re-radiation of RS through plasmonic particles.

agreement with the Rayleigh model. As a consequence, the locally scattered light has the same angular frequency $\boldsymbol{\omega_0}$ as the incident radiation[4]. Thus, by realizing Raman spectroscopy measurement of Raman active molecules, e.g. melamine on spherical Au dimers, according to Equation (3.1) the EF of Raman signal can be expressed as:

$$G_1 \approx \frac{|E_{loc}(\omega_0)|^2}{|E_{inc}(\omega_0)|^2} \quad , \tag{3.19}$$

where $\boldsymbol{E_{loc}(\omega_0)}$ is the locally enhanced electric field on plasmonic particle and $\boldsymbol{E_{inc}(\omega_0)}$ is the magnitude of the electric field component of the incident EM wave. In this way, the

boosted RS signal with angular frequency $\boldsymbol{\omega_{RS}}$ is obtained (see Equation (2.13)). Additionally, it is clearly illustrated for the Au dimer case (Figure 3.4) that the optical properties of noble metals inhere a broad range of natural LSP excitation modes. Subsequently, the second stage of EM mechanism suggests boosting of the RS though re-radiation on plasmon active surfaces. In a similar way, the second input to the enhancement can be given as:

$$G_2 \approx \frac{|E_{loc}(\omega_{RS})|^2}{|E_{RS}(\omega_{RS})|^2} \quad . \tag{3.20}$$

Here, $\boldsymbol{E_{RS}(\omega_{RS})}$ is the amplitude of the electric field component of RS and $\boldsymbol{E_{loc}(\omega_{RS})}$ is the locally enhanced field due to re-radiation effect on plasmonic structures.

It should be emphasized that the re-radiation of RS is accomplished for EM wave with angular frequency of $\boldsymbol{\omega_{RS}}$. In fact, the RS contains spectroscopically rich information about the vibrational modes of the molecule through the shifts in angular frequency $\boldsymbol{\omega_0}$ of incident illumination. Hence, in reality the $\boldsymbol{\omega_{RS}}$ value represents a set of angular frequencies (see Figure 2.5). Now, taking into account that the LSP excitation is actually wavelength dependent (Figure 3.4), the second step of the EM boosting process would result in diversified EF for a distinct $\boldsymbol{\omega_{RS}}$ value. This means that for a Raman active molecule, the original Raman spectrum would be distorted in the surface-enhancement process. The change in fingerprint spectrum would be determined by the LSP behaviour of the plasmonic surface.

To conclude, a complete EF for a particular vibrational mode obtained from both of the contributions is given as:

$$EF = \frac{I_{SERS}}{I_{Raman}} \approx G_1 G_2 = \frac{|E_{loc}(\omega_0)|^2}{|E_{inc}(\omega_0)|^2} \frac{|E_{loc}(\omega_{RS})|^2}{|E_{RS}(\omega_{RS})|^2} \quad . \tag{3.21}$$

This formulation describes the EF achieved on a single molecule. For practical applications, it is more accurate to consider the number of probed molecules and local field distribution[3,4,22]. Nevertheless, Equation (3.21) provides an illustrative representation of the EM boosting mechanism of the surface-enhanced RS phenomenon.

References

(1) Van Duyne, R. P. *Chem. Biochem. Appl. lasers* **1979**, *4*, 101.

(2) Fleischmann, M.; Hendra, P. J.; McQuillan, A. J. *Chem. Phys. Lett.* **1974**, *26* (2), 163–166.

(3) Stiles, P. L.; Dieringer, J. A.; Shah, N. C.; Van Duyne, R. P. *Annu. Rev. Anal. Chem.* **2008**, *1* (1), 601–626.

(4) Ding, S.-Y.; You, E.-M.; Tian, Z.-Q.; Moskovits, M. *Chem. Soc. Rev.* **2017**, *46* (13), 4042–4076.

(5) Otto, A. *Appl. Surf. Sci.* **1980**, *6* (3–4), 309–355.

(6) Campion, A.; Ivanecky, J. E.; Child, C. M.; Foster, M. *J. Am. Chem. Soc.* **1995**, *117* (47), 11807–11808.

(7) Kiefer, W. *Surface enhanced Raman spectroscopy: analytical, biophysical and life science applications*; John Wiley & Sons, 2011.

(8) Wooten, F. *Optical properties of solids*; Academic press, 2013.

(9) Etchegoin, P. G.; Le Ru, E. C.; Meyer, M. *J. Chem. Phys.* **2006**, *125* (16), 164705.

(10) Maier, S. A. *Plasmonics: fundamentals and applications*; Springer Science & Business Media, 2007.

(11) Schulz, L. G. *Adv. Phys.* **1957**, *6* (21), 102–144.

(12) Mishchenko, M. I.; Hovenier, J. W.; Travis, L. D. *Light scattering by nonspherical particles: theory, measurements, and applications*; Academic press, 1999.

(13) Creighton, J. A.; Blatchford, C. G.; Albrecht, M. G. *J. Chem. Soc. Faraday Trans. 2* **1979**, *75*, 790.

(14) Jackson, J. D. *Electrodynamics*; Wiley Online Library, 1975.

(15) Griffiths, D. J. *Introduction to Electrodynamics*; Prentice Hall, 1999.

(16) Geddes, C. D. *Reviews in Plasmonics 2016*; Springer, 2017.

(17) Wriedt, T. Springer, Berlin, Heidelberg, 2012; pp 53–71.

(18) Hutter, E.; Fendler, J. H. *Adv. Mater.* **2004**, *16* (19), 1685–1706.

(19) Mayer, K. M.; Hafner, J. H. *Chem. Rev.* **2011**, *111* (6), 3828–3857.

(20) Taflove, A.; Hagness, S. C. *Computational electrodynamics: the finite-difference time-domain method*; Artech house, 2005.

(21) Hong, Y.; Huh, Y.-M.; Yoon, D. S.; Yang, J. *J. Nanomater.* **2012**, *2012*, 1–13.

(22) Ding, S.-Y.; Yi, J.; Li, J.-F.; Ren, B.; Wu, D.-Y.; Panneerselvam, R.; Tian, Z.-Q. *Nat. Rev. Mater.* **2016**, *1* (6), 16021.

(23) Le, K. Q.; Alù, A.; Bai, J. *J. Appl. Phys.* **2015**, *117* (2), 23118.

4 PLASMONIC NP STRUCTURES

Since its discovery in 1970's[1], surface-enhanced RS gradually attracted interest as a spectroscopic method for various practical applications. First of all, due to the quenching effect of fluorescent molecules on conducting surfaces, the commonly encountered background issue in Raman spectroscopy was resolved using surface-enhanced Raman spectroscopy (SERS) technique[2]. Furthermore, SERS active surfaces (plasmonic structures) has crucial impact when it is employed for molecular sensing. With the advances in nano-fabrication and chemical synthesis methodologies, a broad variety of plasmonic structures including colloidal solution of nanoparticles, thin film of nanoparticle aggregates and highly ordered nanostructures obtained via lithography\imprint technology developed[3–5]. However, depending on the practical utilization of SERS there is an emerging need to evaluate the performance of active surfaces.

The sensing platform, proposed in this PhD thesis, should facilitate qualitative as well as quantitative analysis of analytes in a sample suspension. The SERS technique is highly sensitive, even single molecule detection has been reported[6]. This is achieved via SERS active surfaces with tremendously high localized EF. However, in most of the cases, due to errors in fabrication and as a result local variations in geometry of plasmonic structures, localized high EF are not uniform. This is originating from the near-field properties of LSP excitation which becomes uncontrolled for e.g. aggregated particles with sub-nm gap distances[7]. Alternatively, electron-beam lithography processes can be exploited to achieve highly ordered SERS active substrates[8,9]. But, in that case, one

should consider the ease and cost of the fabrication procedure. For quantitative assessment of analyzed sample, quality parameters for the active SERS surfaces can be formulated. Primarily, a SERS substrate should exhibit EF above 10^5 to achieve the desired sensitivity[7]. Further, quantitative study in SERS requires statistical treatment of the data, hence the EF should be uniform in macroscale with variations of less than 20%. Next, the fabrication process should be reproducible, easy to perform and cheap. Lastly, the plasmonic surface should be clean (free of contamination e.g. arising from fabrication) and provide low interfering SERS background[10].

In this chapter, the sensing tool, metal coated nanopillar SERS substrates which was employed in this PhD work will be presented. Also, complementary utilization of NP SERS substrates will be discussed.

4.1 Fabrication of Metal Coated Si NP Structures

The fabrication procedure for plasmonic NP structures[11] is based on a modified black Si etching process. In our research group, over the past years, multiple NP based SERS substrates have been developed. They include optimizations of LSP excitation modes[12] and density, height of NPs for uniformity of EF[12–14], flexibility in terms of base material (Si, SiO_2, polymeric materials) which eventually provides versatility of NP based SERS substrates for various practical sensing implementations[15–18]. More importantly, the fabrication technique is maskless. This means that throughout the process, costly lithography steps are not implemented. In addition to that, the overall fabrication procedure for metal coated Si NP surfaces yield batch to batch reproducibility in terms of plasmonic properties[11,13].

In general, the fabrication of Si NP SERS substrates consists of three main steps. The overview of the procedure is shown in Figure 4.1. First, NP structures (~50-80 nm

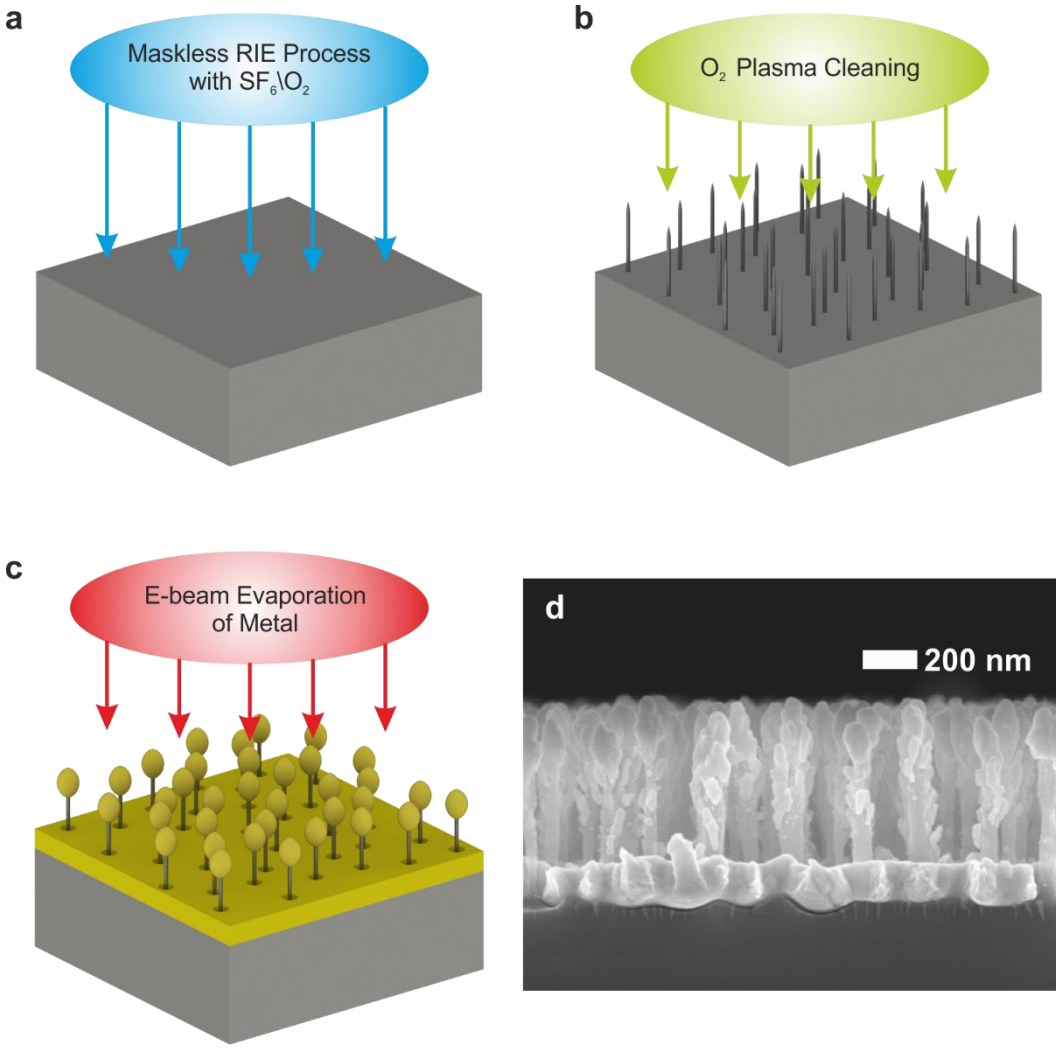

Figure 4.1 Summary for fabrication process of Si base metal coated NP structures. (a) Maskless RIE of Si surface using $SF_6\backslash O_2$ process gasses. (b) Upon completion, NPs on Si surface are obtained and the contaminants from RIE step are removed by O_2 plasma cleaning procedure. (c) Metallization step. Using one of the traditional deposition techniques e.g. electron-beam evaporation, the desired thickness of metal is obtained on Si NPs. (d) SEM image Si NP structures with Au caps achieved via electron-beam evaporation method.

wide) are obtained on a Si wafer using maskless reactive ion etching (RIE) technique with $SF_6\backslash O_2$ process gasses (Figure 4.1a). The RIE is a very delicate method, and by carefully

tuning the process parameters, various micro and nanostructures can be obtained. Thus, the parameters of RIE can be adjusted to achieve different pillar heights and densities[11]. Usually, the etching time is linearly correlated with the NP's height and by manipulating the pressure in the etching chamber, the density of NPs can be altered. A SERS substrate should demonstrate low background signal. Therefore, the RIE of Si is followed by an O_2 plasma cleaning of the surface to eliminate interference of sulphur-fluoride based etching by-products[14] (Figure 4.1b). Lastly, the plasmonic property of Si NPs is obtained by a metallization step (Figure 4.1c). Using a conventional deposition technique, for instance the electron-beam evaporation technique, noble metals (e.g. Au, Ag or Al) with a desired thickness are applied on the NP surface. The final morphology of metal coated (in this case 160 nm of Au via electron-beam method) Si NPs with ~400 nm height is depicted in Figure 4.1d. The image was acquired via scanning electron microscopy (SEM) technique.

Different means of metal deposition would develop variations in morphology of the metal on the NPs. For instance, using magnetron sputtering of Au on NP structures results in uniform coating of the metal while the electron-beam evaporation technique facilitates formation of "caps" on top side of NPs[11]. Consequently, the LSP excitation modes and SERS performance are affected by the alterations in the metal coating. In the following deliberations, the NP structures achieved by directional e-beam evaporation technique, will be considered.

4.2 Leaning Effect of NP Structures

Normally, the applications of fluid samples on SERS substrates are performed by placing a droplet on the surface. According to wettability properties of the liquid towards the nanostructured surface, the sample would locally pin on the applied region or spread across the dry regions and finally evaporate. However, for the case with the NP structures, by tuning the mechanical properties (e.g. stiffness) through modification of the

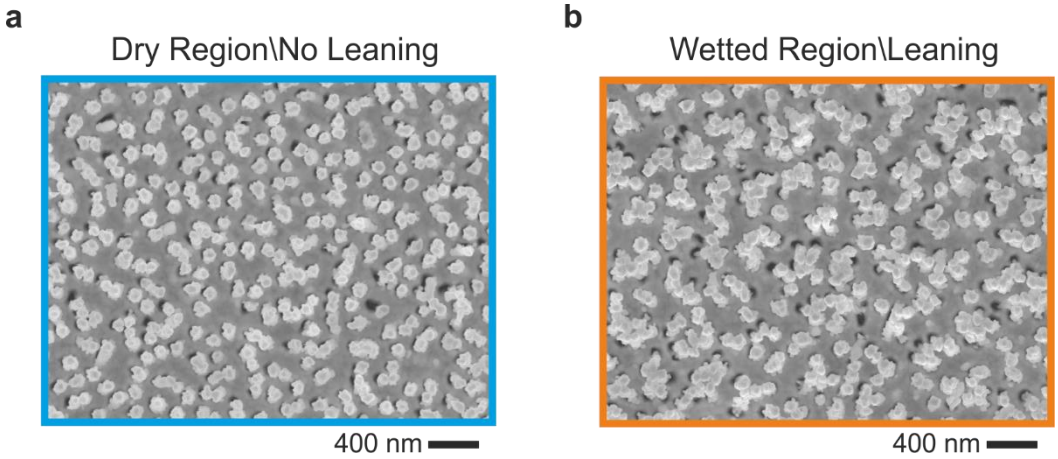

Figure 4.2 Clustering of NPs induced by capillary forces. (a) Top view SEM image of dry region of the SERS substrate, the leaning effect of NPs is not observed. (b) Wetted region, the SEM image was captured right after the evaporation of fluid. The capillary forces during the evaporation process, promoting clustering of the structures. The Si NPs were 400 nm in height and deposited Au thickness was 160 nm.

NPs geometry, a clustering or self-assembly of NPs with the nearest neighbors can be achieved (compare Figure 4.2a the nonwetted region and Figure 4.2b the area exposed to the liquid). In a straightforward way, this can be promoted by tuning the height of NPs via RIE time. This clustering or leaning effect of NPs is greatly dependent on surface tension of the applied liquid sample. Thus, throughout the liquid sample evaporation process, due to capillary action on the nanotextured surface[11], the NPs at the localized spots are pulled towards each other. As per observations reported in various studies with analogous NP SERS substrates, water, ethanol, acetone and other commonly used solvents are facilitating clustering effect[46,49]. Such mechanical self-clustering process would eventually result in formation of sub-nm gap sizes and as a consequence highly localized field enhancements, “hot-spots” as it was shown for the spherical dimer case (Figure 3.4). In Section 4.3, the optical properties of NP structures will be elaborated.

4.3 Plasmonic Properties of NP Substrates

In Section 3.3, it was shown that the LSP excitation modes as well as localized field enhancement through the scattering effect on conducting particles are significantly dependent on the material, geometric properties and arrangement of distinct particles. Similarly, plasmonic properties of NP structures are considerably determined by the cavity mode, a narrow range LSP excitation originating from the metal cap-Si NP interface[12]. By modifying the Si NP diameter and correspondingly changing the gap size of the metal cap, the cavity mode of LSP excitation can be tuned. Nevertheless, due to the errors in RIE process, in reality the NP diameter varies in microscopic regions. For instance, using dark-field instrument which allows to probe scattering on large areas, the distinct plasmonic modes are overlapped resulting in a broader LSP response. On top of that, the leaning effect promotes generation of hybridized mode which is achieved through interaction of LSP modes on diverse NPs[12]. An example for that is demonstrated in Figure 4.3a where experimental dark-field study on Ag coated Si NP structures were conducted. Such broad range LSP resonance response is very attractive for SERS based sensing systems. Depending on the medium, to avoid interferences like fluorescence emission, the excitation laser wavelength of Raman spectrometer can be selected within the LSP resonance band. In Figure 4.3b, simulated electric field enhancement distribution on dimer structure of 40 nm wide Si NP and 310 nm in height, 124 nm wide Ag caps excited using various illumination wavelengths are shown. Taking into account the EM enhancement mechanism elaborated in Section 3.4, Figure 4.3b in an illustrative way demonstrates the spatial arrangement of field EF and consequently different LSP resonance modes suitable for molecular probing through SERS. Alternatively, the broad range LSP resonance bands can be tuned by substituting the Ag cap with Au or Al.

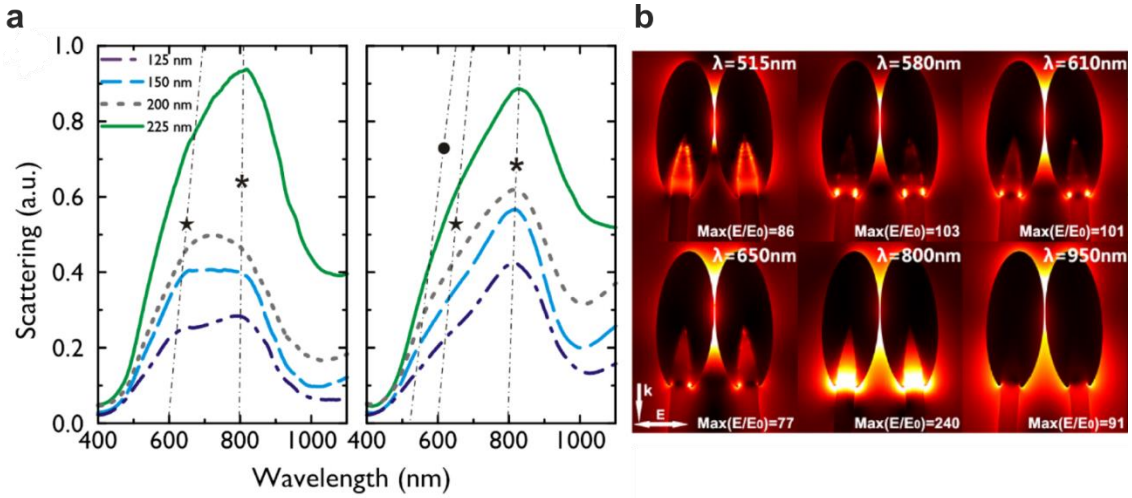

Figure 4.3 LSP excitation and simulated EF distribution on Ag coated NP dimers. (a) Measured dark-field scattering on NP surface before (left) and after the leaning (right) took place. The different colours correspond to distinct Ag deposition thicknesses. The circle, star and asterisks are representing the hybridized, particle and cavity LSP modes respectively. (b) Simulated relative field distribution of NP dimers at various excitation wavelengths. Adapted from reference[12].

The essential criteria for SERS performance relies on EF and its macroscale uniformity. The investigation on Ag capped NP substrates showed that under optimal conditions, EF ~1.3 × 10^8 can be potentially reached. Furthermore, the signal reproducibility or uniformity of EF across a macroscale region (on a 5×5 mm^2 chip) ~14% was reported[14]. In summary, with respect to all quality factors and as compared to the commercially available and reported SERS active surfaces[7], NP substrates exhibit exceptionally good performance as a SERS substrate. Additionally, for in-field applications, the sustainability or shelf-life of the sensor is important. Because of the oxidation effect, Ag coating of NPs can be substituted with Au.

4.4 Sensing Applications using SERS Substrates

SERS is a surface selective sensing technique, and a well-engineered plasmonic substrates can provide tremendous enhancement of RS arising from analyte molecules. However, from a practical point of view, utilization of SERS active substrates in most of the cases, especially for real-life fluid samples, is problematic. Commonly accepted issues to be addressed are; (i) chemically rich environment of the sample[20], (ii) surface selectivity of the sensing platform and lastly[21], (iii) the sample application method onto the substrate surface[22,23]. The first two points are mostly determining the sensitivity and detection limit of a SERS measurement and the last one is correlated with the implementation of a SERS based sensor for molecular quantification purposes. In order to outline the possible obstacles arising from these issues, a specific case will be given as an example.

For instance, a straightforward implementation of SERS technique (applying sample droplet on active surface) for detection of creatinine in human blood serum can be prohibited by macromolecular enzymes and proteins present in the sample[24]. It should be emphasized that the SERS technique is suitable only for molecular systems. The proteins, as an example of macromolecules, would due to their complex molecular structure appear as background in SERS measurements. Moreover, such structures are clogging the plasmon active surfaces, completely blocking the RS from analyte molecules. Thus, the macromolecular clusters are not desired for SERS based platforms.

Moreover, upon sample application on the substrate surface, there is a competing molecular “binding” process onto the SERS active region. The arrangement of analyte molecules will be mostly determined by their surface affinities towards the noble metal (e.g. Au). The surface-enhanced RS phenomenon due to the near-field property of plasmonic structures occurs selectively in proximate regions. Hence, RS of analytes,

which are tightly allocated on a SERS active region, would be preferably enhanced more as compared to molecules with less affinity. In most of the recent SERS based studies with complex media, surface functionalization of the active substrate region was proposed to target specific analytes and to overcome the problem origination from the molecular affinity[25–28]. Of course, such chemical engineering of the surface would eventually increase the sensitivity of the spectroscopic technique. Nevertheless, much more sensitive methods e.g. lateral flow based assays can be developed for detection of specific target analyte in complex mixture[29]. The strength of SERS stands in its specificity for molecular detection. A broad variety of molecules in a complex sample can be identified using a fingerprint spectrum. Hence, the SERS based platforms should target identification and quantification of broad range analyte molecules in complex sample mixture and affinity based issues requires facile and robust sample handling-treatment approaches.

Lastly, the conventional quantification using SERS substrates is achieved through statistical analysis of the data obtained on macroscopic regions (SERS mapping)[17]. The surface-enhanced RS intensity is highly determined by the localized concentration of Raman active molecules in the plasmonic hot-spots. Thus, together with SERS EF uniformity, experimentally consistent spectral signal responses are requiring uniform analyte distribution. The traditional sample droplet application onto the SERS substrate would result in irregular molecular dispersion in macroscale regions known as coffee ring effect[30]. The issue, as reported in multiple studies can be solved via combining SERS based sensing with microfluidics platform. The microfluidics integration allows to perform highly controlled liquid handling operations in an enclosed system eliminating the external influences (e.g. uncontrolled evaporation process)[31]. On this account, a SERS integrated centrifugal microfluidics platform, presented Chapter 0, was developed during the PhD study. An additional obstacle is the SERS signal response with respect to molecular concentration. The quantification using the characteristic non-linear sigmoidal

response named “Langmuir adsorption curve” is challenging for extremely high and low analyte concentrations. In Chapter 0 and 0, the experimental findings addressing above mentioned issues are further elaborated.

4.5 Electrochemical Sensing

Electrochemical (EC) based sensing platforms are dealing with chemical reactions which occur at the electrode-sample interface. The degree of chemical interaction at the interface is measured through the electrical quantities such as current, potential or capacitance[32]. Modern EC based platforms involve a large portfolio of techniques for analyzing chemical reactions in complex matrices. The commonly implemented ones are categorized under the controlled-potential or potentiostatic methods which are carried out on three electrode systems (working, counter and reference electrodes). These techniques are studying the dynamic charge transfers at the liquid sample-electrode interface[32]. In this case, an electric potential is applied between the counter and working electrodes to induce an electron transfer. And the absolute electric potential value at the distinct electrodes is calibrated through a reference electrode. An arising e.g. electrical current can be measured to study the chemical reactions in the sample solution. The overall goal in EC based platforms is to monitor the concentrations of molecular species via chemical reactions or more specifically the redox process of the analytes (Faradaic process)[33]:

$$O + Ne^- \rightleftarrows R \quad , \tag{4.1}$$

at the electrode-sample interface. Here, $\boldsymbol{O}$ and $\boldsymbol{R}$ are the oxidized and reduced compounds, the $\boldsymbol{N}$ represents the number of electrons ($\boldsymbol{e^-}$) transferred to the EC system during the process. The redox process proposes a characteristic potential value $\boldsymbol{V_0}$ at which the reaction becomes possible. Thus, theoretically the concentration ratio between

oxidized $\boldsymbol{C_O}$ and reduced $\boldsymbol{C_R}$ components can be estimated through the applied potential $\boldsymbol{V}$ (Nernst equation)[32]:

$$V = V_0 + \frac{RT}{NF}\, ln\left(\frac{C_O}{C_R}\right) \quad , \tag{4.2}$$

where $\boldsymbol{R}$ stands for universal gas constant (8.314 $J \times K^{-1} \times mol^{-1}$), $\boldsymbol{T}$ temperature of the system and $\boldsymbol{F}$ is the Faraday constant (69.487 C). The resultant current $\boldsymbol{I}$ (Faraday current) which provides information about rate of the redox process is subsequently measured for further EC based characterization of the sample solution. On this account, several techniques such as cyclic voltammetry (CV) or amperometry can be individually deployed to extract information about the quantitative composition of molecular species in the sample solution. CV which implies dynamic study of current in the electrode system versus varying electric potential is the most straightforward and basic method to obtain qualitative assessment of the redox reaction. In addition to that, the quantification of the analyte can be accomplished via the amperometric technique where current response over time is studied at applied constant electric potential.

Instead of a tedious statistical SERS data analysis, as an alternative complementary EC techniques can be integrated with SERS. Thus, using the molecular specificity of SERS for qualitative assessment of the sample medium and the accuracy of EC based measurements for analyte quantification, a synergistical combination of two platforms can be achieved. A proof-of-concept EC-SERS approach is described in Chapter 0.

References

(1) Fleischmann, M.; Hendra, P. J.; McQuillan, A. J. *Chem. Phys. Lett.* **1974**, *26* (2), 163–166.

(2) Petry, R.; Schmitt, M.; Popp, J. *ChemPhysChem* **2003**, *4* (1), 14–30.

(3) Mosier-Boss, P. *Nanomaterials* **2017**, *7* (6), 142.

(4) Sharma, B.; Frontiera, R. R.; Henry, A.-I.; Ringe, E.; Van Duyne, R. P. *Mater. Today* **2012**, *15* (1–2), 16–25.

(5) Fan, M.; Andrade, G. F. S.; Brolo, A. G. *Anal. Chim. Acta* **2011**, *693* (1–2), 7–25.

(6) Kneipp, K.; Wang, Y.; Kneipp, H.; Perelman, L. T.; Itzkan, I.; Dasari, R. R.; Feld, M. S. *Phys. Rev. Lett.* **1997**, *78* (9), 1667–1670.

(7) Prochazka, M. *Surface-Enhanced Raman Spectroscopy: Bioanalytical, Biomolecular and Medical Applications*; Biological and Medical Physics, Biomedical Engineering; Springer International Publishing, 2015.

(8) Hu, M.; Ou, F. S.; Wu, W.; Naumov, I.; Li, X.; Bratkovsky, A. M.; Williams, R. S.; Li, Z. *J. Am. Chem. Soc.* **2010**, *132* (37), 12820–12822.

(9) Abu Hatab, N. A.; Oran, J. M.; Sepaniak, M. J. *ACS Nano* **2008**, *2* (2), 377–385.

(10) Sharma, B.; Fernanda Cardinal, M.; Kleinman, S. L.; Greeneltch, N. G.; Frontiera, R. R.; Blaber, M. G.; Schatz, G. C.; Van Duyne, R. P. *MRS Bull.* **2013**, *38* (8), 615–624.

(11) Schmidt, M. S.; Hübner, J.; Boisen, A. *Adv. Mater.* **2012**, *24* (10), 11–18.

(12) Wu, K.; Rindzevicius, T.; Schmidt, M. S.; Mogensen, K. B.; Xiao, S.; Boisen, A. *Opt. Express* **2015**, *23* (10), 12965–12978.

(13) Wu, K.; Rindzevicius, T.; Schmidt, M. S.; Thilsted, A. H.; Boisen, A. *J. Raman Spectrosc.* **2017**, *48* (12), 1808–1818.

(14) Wu, K.; Rindzevicius, T.; Schmidt, M. S.; Mogensen, K. B.; Hakonen, A.; Boisen, A. *J. Phys. Chem. C* **2015**, *119* (4), 2053–2062.

(15) Morelli, L.; Andreasen, S. Z.; Jendresen, C. B.; Nielsen, A. T.; Emnéus, J.; Zór, K.; Boisen, A. *Analyst* **2017**, *142* (23), 4553–4559.

(16) Morelli, L.; Zór, K.; Jendresen, C. B.; Rindzevicius, T.; Schmidt, M. S.; Nielsen, A. T.; Boisen, A. *Anal. Chem.* **2017**, *89* (7), 3981–3987.

(17) Palla, M.; Bosco, F. G.; Yang, J.; Rindzevicius, T.; Alstrom, T. S.; Schmidt, M. S.; Lin, Q.; Ju, J.; Boisen, A. *RSC Adv.* **2015**, *5* (104), 85845–85853.

(18) Yang, J.; Palla, M.; Bosco, F. G.; Rindzevicius, T.; Alstrøm, T. S.; Schmidt, M. S.; Boisen, A.; Ju, J.; Lin, Q. *ACS Nano* **2013**, *7* (6), 5350–5359.

(19) Durucan, O.; Rindzevicius, T.; Schmidt, M. S.; Matteucci, M.; Boisen, A. *ACS Sensors* **2017**, *2* (10), 1400–1404.

(20) Sun, F.; Hung, H.; Sinclair, A.; Zhang, P.; Bai, T.; Galvan, D. D.; Jain, P.; Li, B.; Jiang, S.; Yu, Q. *Nat. Commun.* **2016**, *7*, 13437.

(21) Bell, S. E. J.; Sirimuthu, N. M. S. *J. Phys. Chem. A* **2005**, *109* (33), 7405–7410.

(22) Lee, M.; Lee, K.; Kim, K. H.; Oh, K. W.; Choo, J. *Lab Chip* **2012**, *12* (19), 3720.

(23) Strehle, K. R.; Cialla, D.; Rösch, P.; Henkel, T.; Köhler, M.; Popp, J. *Anal. Chem.* **2007**, *79* (4), 1542–1547.

(24) Stosch, R.; Henrion, A.; Schiel, D.; Güttler, B. *Anal. Chem.* **2005**, *77* (22), 7386–7392.

(25) Etchegoin, P. G.; Le Ru, E. C. *Phys. Chem. Chem. Phys.* **2008**, *10* (40), 6079.

(26) Liu, T.-Y.; Tsai, K.-T.; Wang, H.-H.; Chen, Y.-H.; Chen, Y.-H.; Chao, Y.-C.; Chang, H.-H.; Lin, C.-H.; Wang, J.-K.; Wang, Y.-L. *Nat. Commun.* **2011**, *2*, 538.

(27) Dinish, U. S.; Yaw, F. C.; Agarwal, A.; Olivo, M. *Biosens. Bioelectron.* **2011**, *26* (5), 1987–1992.

(28) Pekdemir, M. E.; Ertürkan, D.; Külah, H.; Boyacı, İ. H.; Özgen, C.; Tamer, U. *Analyst* **2012**, *137* (20), 4834.

(29) Koczula, K. M.; Gallotta, A. *Essays Biochem.* **2016**, *60* (1), 111–120.

(30) Deegan, R. D.; Bakajin, O.; Dupont, T. F.; Huber, G.; Nagel, S. R.; Witten, T. A. *Nature* **1997**, *389* (6653), 827–829.

(31) Huang, L.; Bian, S.; Cheng, Y.; Shi, G.; Liu, P.; Ye, X.; Wang, W. *Biomicrofluidics* **2017**, *11* (1), 11501.

(32) Wang, J. *Analytical electrochemistry*; John Wiley & Sons, 2006.

(33) Heineman, W. R.; Kissinger, P. T. *Anal. Chem.* **1980**, *52* (5), 138–151.

5 CENTRIFUGAL MICROFLUIDICS

Miniaturized microfluidic systems have attracted great interest for various point-of-care, environmental and food safety applications. The advantage of microfluidics based platforms over the existing diagnostic techniques are their unique capabilities in liquid sample manipulations, possible in-field employment and sensor integration. Thus, complicated laboratory fluid handling steps such as metering, mixing, valving and sample transport can be efficiently accomplished in an automated way without any human interference[1,2]. In a conventional microfluidics device, the fluid is driven through dynamic control of the pressure in an enclosed chip. This is primarily achieved by active utilization of external pumps and in this way, the hydrodynamic properties such as sample flow rate are precisely regulated[3,4]. However, as the practical requirements for sample pre-treatment expand, the design and fabrication processes of the multifunctional microfluidic device are becoming tedious and difficult to realize. Moreover, most of the point-of-care applications are necessitating multiplex analysis of the sample. As a result, the final device may consist of a large number of external pumps, tubings connecting to microfluidic chip and sophisticated structures for fluid handling[5,6].

These practical complications can be partially resolved by centrifugal microfluidics[7,8]. In contrast to conventional microfluidics, the centrifugal platform does not require any external pumping devices and tubings. The fluid management is realized through inertial forces acting on fluids which are promoted by rotation of the microfluidic disc platform[7]. Furthermore, by controlled rotation of the disc, precise and automated fluid handling procedures are obtained. Additionally, considering its geometrical

symmetry, the platform is suitable for multiplexing and performing simultaneous microfluidic processes[9].

In this chapter, the sample handling-treatment element of a SERS based sensing platform, centrifugal microfluidics will be presented.

5.1 Inertial Forces

The fluid transport and handling operations in centrifugal microfluidics are prominently facilitated through pseudo inertial (or fictitious) forces. The fictitious forces are characterizing a non-inertial frame of reference for which the classical Newton laws are inapplicable. Thus, a rotating (or for broader definition with an angular acceleration) disc which is a non-inertial frame of reference, will be influenced by these forces[8,10]. To illustrate this, a specific idealized case of a rotating disc (spinning about its center) with angular frequency $\vec{\boldsymbol{\omega}}(\boldsymbol{t})$ and point like mass $\boldsymbol{dm}$ of e.g. fluid on the disc with velocity $\vec{\boldsymbol{V}}$ as shown in Figure 5.1a will be taken into account. Further, interaction of the point mass with the disc and surrounding medium as well as the fluid properties e.g. viscosity will be neglected. In this way, the resultant inertial force on the point mass will be:

$$d\vec{F}_{inertial} = dm\left(2\left[\vec{V}\times\vec{\omega}\right] + \left[\vec{\omega}\times\left[\vec{r}\times\vec{\omega}\right]\right] + \left[\vec{r}\times\left(\frac{d\vec{\omega}}{dt}\right)\right]\right) \quad , \qquad (5.1)$$

where $\vec{\boldsymbol{r}}$ is position vector of the point mass, the first term in general bracket stands for Coriolis, second for centrifugal and last one for the Euler forces (Figure 5.1b). In principle, considering that the practical liquid flow rates in microfluidics systems are generally insignificant as compared to angular frequency and acceleration of the disc, the Coriolis force component can be neglected[7]. Thus, in a straightforward way, by tuning

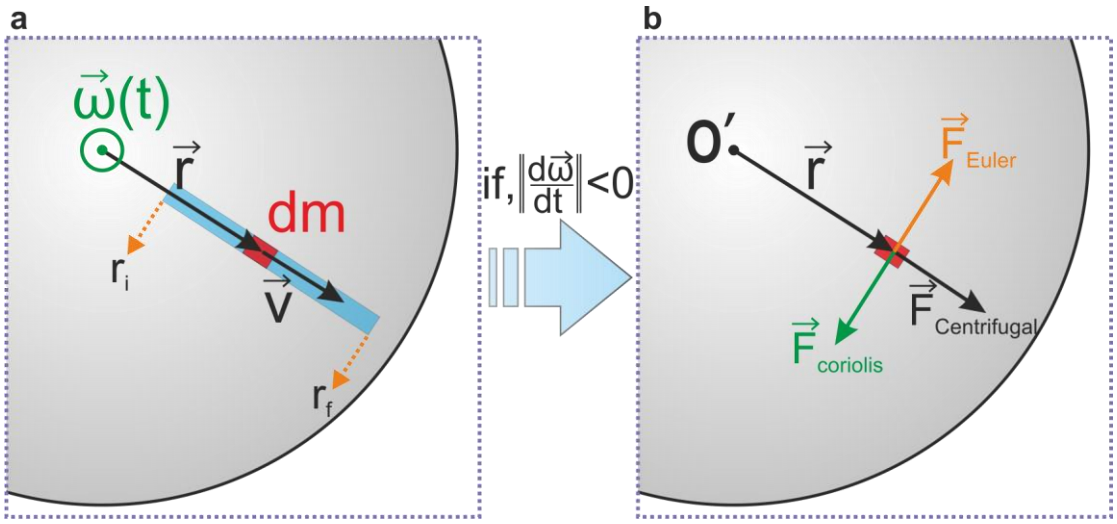

Figure 5.1 Pseudo forces in centrifugal microfluidics platform. (a) A disc, rotating about its center with angular frequency $\vec{\omega}$ and with a tiny channel from r_i to r_f in radial direction filled with fluid. (b) Inertial forces on a point like mass dm stimulated through the rotational motion of the disc.

the spinning parameters of the microfluidic disc platform and consequently the centrifugal and Euler forces, desired fluid operations can be performed.

An important parameter for microfluidics based system is the driving pressure on the fluids. In conventional devices, the precise dynamic liquid transport is realized through controlled pressure difference acquired via a pumping equipment. Similarly, in enclosed centrifugal microfluidics platform, the external pressure is applied through the inertial forces. The previous case can serve as a representative example to demonstrate this. More specifically, considering a tiny microfluidic channel filled with fluid (from r_i to r_f) as shown in Figure 5.1a, the pressure difference between the two ends of liquid level would be:

$$\Delta P = \int_{r_i}^{r_f} \frac{\left(d\vec{F}_{inertial} \cdot d\vec{r}\right)}{dV} \quad , \tag{5.2}$$

where $\boldsymbol{dV}$ term represents differential volume of the point like mass $\boldsymbol{dm}$. Next, for simplicity the rotation of the disc can be assumed to be constant which implies that the angular acceleration would be zero. Therefore, the Euler term in Equation (5.1) will not be considered. In addition to that, with respect to previous assumption with negligible Coriolis force component, the pressure difference in Equation (5.2) caused by centrifugal force can be given in a following way:

$$\Delta P = \frac{\rho\omega^2}{2}\left({r_f}^2 - {r_i}^2\right) \quad . \tag{5.3}$$

Here, $\boldsymbol{\rho}$ represents the density of the fluid. The Equation (5.3) is useful when estimating an equilibrium condition of fluid arrangement at constant rotational frequency. Hence, the essential primary optimizations of microfluidic structures can be achieved using this analytical formulation.

The dynamic fluid handling operations are demanding specificity in force direction to guide the sample through the microfluidic structures in a required way. For this reason, as an example, the Euler force component is employed to regulate the force action on fluids in angular direction. Further, auxiliary fluid manipulations in a centrifugal platform are accomplished through fluid-surrounding medium interactions. In the following sections, some basic examples for those interactions will be provided.

5.2 Pneumatic Pumping

In Section 5.1 the inertial forces acting on fluids in a rotating/accelerating disc platform were presented. It should be emphasized that each force component in Equation (5.1) can be altered to govern the liquid. However, by employing the pseudo forces, liquid flow towards the center of the disc or in other words, opposite to the radial direction cannot be realized[11]. This suggests that the subsequent liquid configurations in microfluidic structures, accomplished by means of Euler and centrifugal forces, are not reversible. On that account, various supplementary techniques are utilized together with inertial forces in order to obtain higher degree of freedom of fluid management in a

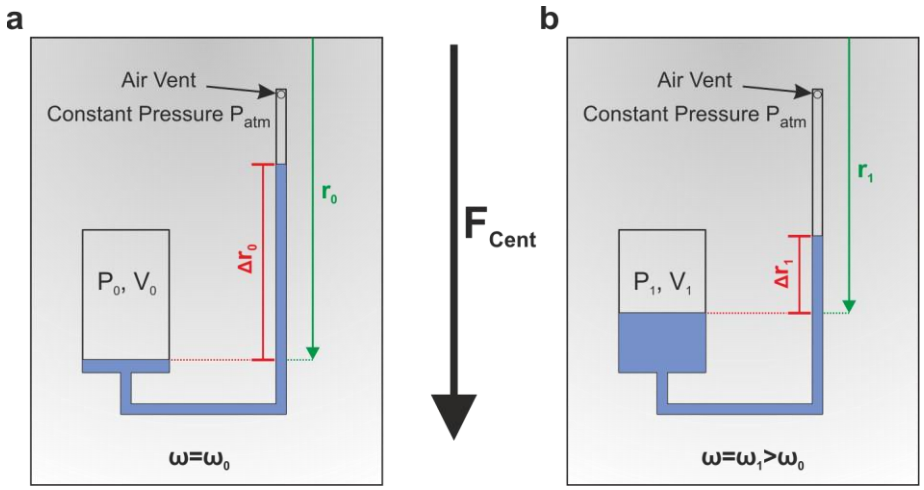

Figure 5.2 Pneumatic pumping principle in centrifugal microfluidics. (a) A simplified enclosed microfluidics system which consists of a sealed chamber (left) and a tiny channel with an air vent which is linked to it (right). The stationary liquid arrangement at the rotational frequency $\boldsymbol{\omega_0}$ is shown. (b) Similarly, the equilibrium condition for the fluid distribution at a higher spinning frequency $\boldsymbol{\omega_1}$ is depicted. As a result, the liquid level and air pressure in the sealed pneumatic chamber are increased. The associated geometrical and thermodynamical parameters are labelled in the figure.

centrifugal platform. One commonly exploited method is the pneumatic pumping which is fundamentally accomplished through compression (or decompression) of the air in an enclosed microfluidic chamber. Thus, by manipulating the air pressure in a pneumatic chamber, additional dynamic action on fluid samples can be obtained[11–13]. To interpret the basic working principle of the technique, the microfluidic model presented in Figure 5.2 will be given as an example. Here, a straightforward microfluidic design containing a sealed chamber (pneumatic chamber) interconnected with an air vent though a tiny channel is shown. Further, a hypothetical liquid configuration for a specific rotational frequency $\boldsymbol{\omega_0}$ of the disc at the equilibrium condition is depicted in Figure 5.2a. The stationary arrangement is summarized through thermodynamic properties of the compressed air in the pneumatic chamber (pressure $\boldsymbol{P_0}$ and corresponding volume $\boldsymbol{V_0}$) and the radial height parameters ($\Delta\boldsymbol{r_0}$ and $\boldsymbol{r_0}$) of the homogeneous liquid in the microfluidic structures. With respect to the Equation (5.3), the analytical form of this steady state, as well as the relationship between liquid configuration and the thermodynamical properties of the pneumatic chamber can be formulated in the following way:

$$\Delta P = P_0 - P_{atm} = \frac{\rho\omega_0^2}{2}\,\Delta r_0(2r_0 - \Delta r_0) \quad . \tag{5.4}$$

Eventually, this suggests that the action of the compressed air in pneumatic chamber ($\boldsymbol{P_0 > P_{atm}}$) is compensated through liquid height difference at both ends of the fluid (centrifugal pressure, see Section 5.1). As a remark, the capillary action which occurs in the narrow microfluidic channels was not included in the model. The effect will be elaborated in the following Section 5.3.

Certainly, by applying additional centrifugal pressure (e.g. by increasing the angular frequency of the disc to $\boldsymbol{\omega_1}$ and keeping the liquid volume constant) the thermodynamical properties of compressed air and the liquid configuration would change. Thus, considering a quasi-static acceleration of the disc, in a similar manner the equilibrium state at angular frequency $\boldsymbol{\omega_1}$ can be given as (Figure 5.2b):

$$\Delta P = P_1 - P_{atm} = \frac{\rho \omega_1^2}{2} \Delta r_1 (2r_1 - \Delta r_1) \quad . \tag{5.5}$$

Since the acceleration process of the disc was assumed to be quasi-static (isothermal procedure), the dependence of thermodynamical parameters between two distinct stationary conditions is described through the Boyle-Mariotte's law[14]:

$$P_0 V_0 = P_1 V_1 \quad . \tag{5.6}$$

Moreover, this thermodynamic process is theoretically reversible (due to dissipative forces, practically it is not fully reversible) which suggests that by slowly altering the rotational frequency of the disc the liquid heights can be precisely regulated[15].

5.3 Capillary Valving

A complementary effect which has sufficient impact on microfluidic handling procedures is the capillary action of liquids in narrow spaces (e.g. a tiny channel). This surface phenomenon is highly dependent on fluid-environment interactions. In this way, under influence of adhesive and cohesive forces between liquid and e.g. microfluidic channel wells, the internal pressure value can be varied[16–18]. For instance, if the fluid possesses hydrophilic properties towards the surface of the microfluidic channel (dominating adhesive forces), the internal fluid pressure value is lowered. In contrast to that, hydrophobic interactions would imply increase in internal pressure of the liquid.

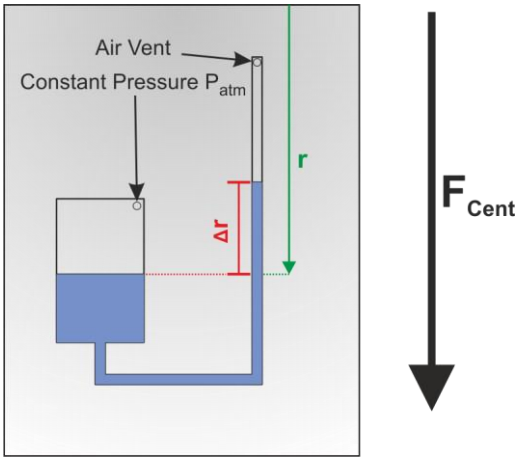

Figure 5.3 Capillary action in centrifugal microfluidics. The fluid arrangement at the equilibrium condition for rotational angular frequency $\boldsymbol{\omega}$. Due to air vent openings, the pressure values at both liquid ends are constant. The capillary interaction (in this case hydrophilic) facilitates rise of fluid height in a narrow channel which has a smaller width than the chamber.

Considering the microfluidic design summarized in Figure 5.3 and relatively small channel width $\boldsymbol{d}$, the capillary rise or capillary pressure can be analytically defined using Young-Laplace equality[19]:

$$\Delta P = \frac{\rho\omega^2}{2}\,\Delta r(2r - \Delta r) = \frac{4\alpha\, cos\theta}{d}\,, \qquad (5.7)$$

where $\boldsymbol{\alpha}$ is the surface tension of the fluid and $\boldsymbol{\theta}$ is the contact angle at the fluid-solid interface. Subsequently, by regulating the centrifugal pressure in Equation (5.7), the liquid level can be adjusted. The effect of capillary rise is frequently utilized in a centrifugal microfluidic platform for valving techniques. Thus, a carefully designed microfluidic channel (geometrical shape, dimensions, material and possible coating) can

serve as a conditional (rotational parameters) fluid transfer unit e.g. from one chamber to another[8,11].

5.4 Design and Fabrication of Microfluidic Discs

In an accurate way, microfluidic structures for specific sample handling operations are designed using computer modelling techniques. Accordingly, by carrying out computational simulations of fluid interactions with surrounding media, an estimated fluid behavior and consequently an optimization process of the microfluidic structure geometry is performed. Following that, using fabricated prototype discs, additional and final adjustments in structure morphology are made[20,21]. Nevertheless, the computational techniques, specifically complete 3-dimensional fluidic simulations are time consuming and it is often the case that the results are depicting inaccurate microfluidic response (due to errors in computational parameters).

Throughout this PhD study, the design procedure for microfluidic structures was conducted in an alternative way. First of all, using the analytical assumptions described in Sections 5.1, 5.2 and 5.3, a rough approximation of a microfluidic model for desired handling operations was obtained. Further, by taking advantage of the rapid prototyping fabrication technique, described in Chapter 0, the optimization and fine adjustment of microfluidic designs were achieved experimentally. The discs were produced via step-by-step assembly of laser cut polymeric discs (e.g. poly (methyl methacrylate)-PMMA) and patterned pressure sensitive adhesive (PSA) layers. The complete SERS integrated centrifugal microfluidic discs are produced within 20-30 min. Lastly, the desired fluid handling operations are tested in an optical spin stand where real-time images of the disc are captured during the centrifugation process. After each design and test, necessary adjustments for desired fluidic operations were implemented for the next prototypes.

Finally, the testified and optimized design can be produced in a facile and robust way using mass production methods. Injection molding as an exemplary mass production technique is demonstrated in Chapter 0.

References

(1) Whitesides, G. M. *Nature* **2006**, *442* (7101), 368–373.

(2) Squires, T. M.; Quake, S. R. *Rev. Mod. Phys.* **2005**, *77* (3), 977–1026.

(3) Stone, H. A.; Stroock, A. D.; Ajdari, A. *Annu. Rev. Fluid Mech.* **2004**, *36* (1), 381–411.

(4) Beebe, D. J.; Mensing, G. A.; Walker, G. M. *Annu. Rev. Biomed. Eng.* **2002**, *4* (1), 261–286.

(5) Wang, G.; Ho, H.-P.; Chen, Q.; Yang, A. K.-L.; Kwok, H.-C.; Wu, S.-Y.; Kong, S.-K.; Kwan, Y.-W.; Zhang, X. *Lab Chip* **2013**, *13* (18), 3698.

(6) Strohmeier, O.; Keller, M.; Schwemmer, F.; Zehnle, S.; Mark, D.; von Stetten, F.; Zengerle, R.; Paust, N. *Chem. Soc. Rev.* **2015**, *44* (17), 6187–6229.

(7) Gorkin, R.; Park, J.; Siegrist, J.; Amasia, M.; Lee, B. S.; Park, J.-M.; Kim, J.; Kim, H.; Madou, M.; Cho, Y.-K. *Lab Chip* **2010**, *10* (14), 1758.

(8) Ducrée, J.; Haeberle, S.; Lutz, S.; Pausch, S.; Stetten, F. von; Zengerle, R. *J. Micromechanics Microengineering* **2007**, *17* (7), S103–S115.

(9) Nolte, D. D. *Rev. Sci. Instrum.* **2009**, *80* (10), 101101.

(10) Burger, R.; Ducrée, J. *Expert Rev. Mol. Diagn.* **2012**, *12* (4), 407–421.

(11) Gorkin, R.; Clime, L.; Madou, M.; Kido, H. *Microfluid. Nanofluidics* **2010**, *9* (2–3), 541–549.

(12) Mark, D.; Metz, T.; Haeberle, S.; Lutz, S.; Ducrée, J.; Zengerle, R.; von Stetten, F. *Lab Chip* **2009**, *9* (24), 3599.

(13) Abi-Samra, K.; Clime, L.; Kong, L.; Gorkin, R.; Kim, T.-H.; Cho, Y.-K.; Madou, M. *Microfluid. Nanofluidics* **2011**, *11* (5), 643–652.

(14) De Groot, S. R.; Mazur, P. *Non-equilibrium thermodynamics*; Courier Corporation, 2013.

(15) Gorkin, R.; Nwankire, C. E.; Gaughran, J.; Zhang, X.; Donohoe, G. G.; Rook, M.; O'Kennedy, R.; Ducrée, J. *Lab Chip* **2012**, *12* (16), 2894.

(16) Chen, J. M.; Huang, P.-C.; Lin, M.-G. *Microfluid. Nanofluidics* **2008**, *4* (5), 427–437.

(17) Siegrist, J.; Gorkin, R.; Clime, L.; Roy, E.; Peytavi, R.; Kido, H.; Bergeron, M.; Veres, T.; Madou, M. *Microfluid. Nanofluidics* **2010**, *9* (1), 55–63.

(18) Zeng, J.; Banerjee, D.; Deshpande, M.; Gilbert, J. R.; Duffy, D. C.; Kellogg, G. J. In *Micro Total Analysis Systems 2000*; Springer Netherlands: Dordrecht, 2000; pp 579–582.

(19) Cho, H.; Kim, H.-Y.; Kang, J. Y.; Kim, T. S. *J. Colloid Interface Sci.* **2007**, *306* (2), 379–385.

(20) Rasmussen, A.; Mavriplis, C.; Zaghloul, M. E.; Mikulchenko, O.; Mayaram, K. *Sensors Actuators A Phys.* **2001**, *88* (2), 121–132.

(21) Chen, X.; Cui, D.; Liu, C.; Li, H.; Chen, J. *Anal. Chim. Acta* **2007**, *584* (2), 237–243.

Available online:
https://pubs.acs.org/doi/abs/10.1021/acssensors.7b00499

6 NANOPILLAR FILTERS FOR SERS

Original title: Nanopillar filters for Surface-Enhanced Raman Spectroscopy

Onur Durucan[1,*], Tomas Rindzevicius[1], Michael Stenbæk Schmidt[1], Marco Matteucci[1], and Anja Boisen[1]

[1]Technical University of Denmark, Department of Micro-and Nano Technology, Kgs. Lyngby, 2800, Denmark

**onurd@nanotech.dtu.dk*

Published in ACS Sens., 2017, 2 (10), pp 1400–1404.

Abstract

We present a simple, robust and automated molecule extraction technique based on a centrifugal microfluidic platform. Fast and facile extraction of a food adulterant (melamine) from a complex sample medium (milk) on a SERS substrate is demonstrated. The unique characteristic of the detection method is the obtained "filter paper/chromatographic" effect which combines centrifugal force and wetting properties of the SERS substrate. The work addresses issues related to SERS-based detection of analytes in complex media, which is important for realizing next generation SERS platforms applicable for a broad variety of real-life applications.

Keywords: SERS, Wicking, Microfluidics, Nanopillars, Filtration, Melamine

Unpublished Manuscript

7 NP Structures for SERS Chromatography

Original title: Nanopillar structures for Surface-Enhanced Raman Spectroscopy Chromatography

Onur Durucan[1, *], Kaiyu Wu[1, *], Tomas Rindzevicius[1], Marlitt Viehrig[1], Oleksii Ilchenko[1], Michael Stenbæk Schmidt[1], and Anja Boisen[1]

[1]Technical University of Denmark, Department of Micro-and Nano Technology, Kgs. Lyngby, 2800, Denmark

**onurd@nanotech.dtu.dk, *kaiwu@nanotech.dtu.dk*

Unpublished Manuscript.

Abstract

We demonstrate a new, fully integrated chromatography method for analyzing complex, multicomponent samples, i.e. human urine spiked with paracetamol, using surface-enhanced Raman spectroscopy (SERS). Gold coated silicon nanopillar substrates (Au NP) and disc-based, centrifugal microfluidic platform are combined to manipulate the liquid matrix and simultaneously generate a chromatographic effect on the ~4x4 mm Au NP surface area. Results show that high density (~48 pillars/ μm^{-2}) Au NP structures can be used to effectively separate paracetamol and the main human urine components (urea, uric acid and creatinine) on the substrate for subsequent SERS detection. The Au NP induced chromatographic effect was visualized and analyzed using the multivariate curve resolution-alternative least squares (MCR-ALS) method. The integrated SERS chromatography platform was further utilized for quantitative detection of paracetamol (0-500 ppm) in human urine. By analyzing the analyte surface spreading profiles, a reproducible, linear trend across the entire concentration range was obtained. The new method is an important leap towards developing a fully integrated SERS sensing platform for quantitative, multicomponent analysis of analytes in various biofluids e.g. saliva, blood or urine.

Keywords: SERS, Wicking, Microfluidics, Nanopillars, Chromatography, Urine, Paracetamol

Available online:
https://pubs.acs.org/doi/abs/10.1021/acssensors.7b00783

8 DUAL-FUNCTIONAL EC AND SERS SENSING

Original title: Large-scale, Lithography-free Production of Transparent Nanostructured Surface for Dual-functional Electrochemical and SERS Sensing

Kuldeep Sanger[1,*], Onur Durucan[1,*], Kaiyu Wu[1], Anil Haraksingh Thilsted[1], Arto Heiskanen[1], Tomas Rindzevicius[1], Michael Stenbæk Schmidt[1], Kinga Zor[1] and Anja Boisen[1]

[1]Technical University of Denmark, Department of Micro-and Nano Technology, Kgs. Lyngby, 2800, Denmark

**sakuld@nanotech.dtu.dk, *onurd@nanotech.dtu.dk*

Published in ACS Sens., 2017, 2 (12), pp 1869–1875

Abstract

In this work, we present a dual-functional sensor that can perform surface-enhanced Raman spectroscopy (SERS) based identification and electrochemical (EC) quantification of analytes in liquid samples. A lithography-free reactive ion etching process was utilized to obtain nanostructures of high aspect ratios distributed homogeneously on a 4-inch fused silica wafer. The sensor was made up of three-electrode array, obtained by subsequent e-beam evaporation of Au on nanostructures in selected areas through a shadow mask. The SERS performance was evaluated through surface-averaged enhancement factor (EF), which was ~6.2 x 10^5, and spatial uniformity of EF, which was ~13% in terms of relative standard deviation. Excellent electrochemical performance and reproducibility were revealed by recording cyclic voltammograms. On nanostructured electrodes, paracetamol (PAR) showed an improved quasi-reversible behavior with decrease in peak potential separation (ΔEp ~90mV) and higher peak currents (I_{pa}/I_{pc} ~1), comparing to planar electrodes (ΔEp ~560mV). The oxidation potential of PAR was also lowered by ~80 mV on nanostructured electrodes. To illustrate dual-functional sensing, quantitative evaluation of PAR ranging from 30 µM to 3 mM was realized through EC detection, and presence of PAR was verified by its SERS fingerprint.

9 CONCLUDING REMARKS

In this PhD thesis, applicability of surface-enhanced Raman spectroscopy (SERS) based centrifugal microfluidic platform for sensing applications was investigated. The aim of the platform is to automate sample pre-treatment (e.g. filtration, separation, etc.) procedure and enable quantitative SERS-based analysis of molecular species in chemically rich, complex, real-life samples. As discussed in Chapter 4, it is well-known that this requires (1) reliable and high-performance SERS substrates, (2) advanced sample pre-treatment and dosing techniques. With the recent developments in nanofabrication methods, the first point can be addressed by utilizing highly uniform nanopillar (NP) structures fabricated on large-scale surfaces (4 inch wafers). The gold metal coated NP arrays developed in the Nanoprobes research group exhibit exceptionally good SERS performance. Thus, the focus for the PhD study was on integration of the NP SERS substrate into a microfluidics platform and application development.

The sample handling and pre-treatment steps were accomplished in the SERS integrated centrifugal microfluidics platform (see Chapter 6 and 7). By taking advantage of precise and automated fluid management procedures in microfluidics platform, reproducible incubation of sample onto the NP surface can be obtained. On that account, various microfluidic techniques such as metering, valving and pneumatic pumping were realized. Another crucial impact of the platform is the regulative inertial forces which are facilitated through rotation of the microfluidic discs. By manipulating the rotational parameters and consequently the inertial forces, an optional sedimentation of macromolecular particles in sample suspension (centrifugation) was carried out. In an

illustrative way, this was demonstrated on melamine doped milk solutions under 47.5 Hz rotational frequency of the disc.

The centrifugation process promoted phase separation of the sample with respect to density gradient of the contents. However, the centrifugation as pre-treatment method was not sufficient enough to obtain the required degree of sample purity. Considering the high sensitivity and selectivity of the surface-enhanced Raman scattering (RS) phenomenon, the real-life applications require (i) complete filtration of macromolecules, (ii) separation of distinct analyte species and lastly (iii) uniform analyte dosage on the surface. On this account, the wicking effect caused by capillary interaction of fluid sample and nanotextured surface (NP structures) was employed in the centrifugal platform.

Results in the first study showed that NP structures can be used as nanofilters for pre-treating milk samples which significantly improves melamine detection using SERS (Chapter 6). Macromolecular clusters such as proteins and fats were clogged in the immersion region while the diffusing thin layer of the milk suspension (through capillary wicking) was purified. This was verified using morphological inspection of the NP surface through scanning electron microscopy. Furthermore, the effect facilitated controlled deposition of analyte molecules (artificially doped melamine) onto the NP SERS substrate. The results from experimental SERS mapping on purified region of NP surface indicated that the melamine molecules were uniformly accumulated. Following that, the statistical SERS map studies of analyte peak at 687 cm^{-1} demonstrated that the quantification of melamine concentrations ranging from 10 parts per million (ppm) up to 400 ppm is possible using this technique. Lastly, melamine concentration versus the SERS signal intensity response obtained using the novel sample dosing technique was in agreement with Langmuir adsorption curve which is a characteristic feature of the SERS based sensing platforms.

In the second case study, the aim was to obtain a “chromatographic effect” from paracetamol doped human urine samples directly on the nanopillar SERS substrate for simultaneous SERS detection of the analyte and different urine compounds. Essentially, the main challenge for a reliable SERS based sensing of analytes in a complex matrix arises from the competitive binding effect of sample contents on the SERS active surface. The surface-enhanced RS phenomenon is highly surface sensitive, thus only the molecules which are located in the close vicinity of the active region (electromagnetic “hot-spots”) will contribute to the SERS signal. The distribution of molecular compounds in complex sample suspension on SERS active region is highly determined by their affinities towards the plasmonic surface. Practically, the application of multicomponent sample solution on a SERS substrate without any sample pre-treatment results in selective accumulation of components (molecule species with higher affinity) on SERS active structures. For the “chromatographic effect” described in Chapter 7, wicking phenomenon which proposes gradual diffusion of fluid sample on the NP surface was utilized to segregate molecular species in the multicomponent sample solution. More specifically, along the spreading path of urine solution on the NP substrate, the arrangement of components was determined by their binding property (affinity) towards plasmonic surface (Au). Consequently, the contents were trapped locally on SERS active regions. Further, the experimental SERS studies and the spectral decomposition analysis confirmed that the typical components of human urine such as urea, uric acid, creatinine and the artificially doped paracetamol were successfully separated along the NP SERS substrate. Moreover, a linear concentration dependence of paracetamol with respect to its spectral profile was shown. Accordingly, quantification of paracetamol concentration ranging from 30 to 500 ppm was demonstrated.

Finally, an alternative dual functional sensing approach was experimentally investigated (Chapter 8). The capability of electrochemical (EC) sensors to quantify

analyte molecules through reduction-oxidation reactions and spectral specificity of the SERS technique was combined into a single detection platform. The goal was to explore if the two techniques could complement each other and improve the analyte detection in liquid samples. In order to integrate the two techniques into a single sensing unit, NP-like structures on fused silica suitable for both EC and SERS detection were fabricated and utilized as an active surface. The advantages and limitations of the proposed dual-functioning sensor concept was examined using phosphate-buffered saline (PBS) solution doped with paracetamol. The EC quantification and SERS identification limit was estimated to be 30 µM paracetamol concentration in PBS.

In summary, the thesis presents a number of solutions to address commonly encountered issues associated with SERS based sensors, especially when dealing with real-life samples such as milk, or complex biofluids such as urine. The research conducted during the PhD project is aimed at the development of next generation SERS platforms with automated sample manipulation, pre-treatment and filtration. The suggested methodologies are suitable for a wide range of practical application, and could be further optimized by e.g. tuning the morphology of SERS active structures. Importantly, results showed that the SERS-centrifugal microfluidic platform can be used for multicomponent, label-free and sensitive detection of analyte species in a complex matrix without using any surface functionalization procedures.

DTU Nanotech
Department of Micro- and Nanotechnology

DTU

In this thesis, the summary of research activities conducted throughout the PhD employment from 15th of January 2015 at the Nanoprobes research group (Department of Micro- and Nanotechnology, Technical University of Denmark) is presented. The PhD project was part of the HERMES-High Exponential Rise in Miniaturized cantilever-like Sensing project founded by European Research Council (ERC), grant no. 320535.

DTU Nanotech
Ørsteds Plads, building 345C
DK-2800 Kgs. Lyngby
http://www.nanotech.dtu.dk/

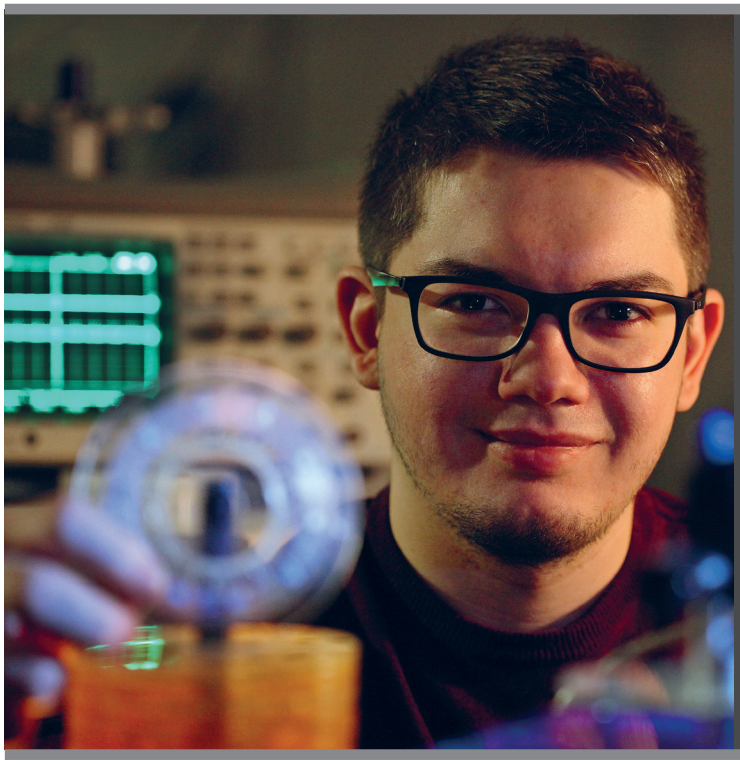

Published by:
DTU Nanotech
Department of Micro- and Nanotechnology
Technical University of Denmark
Ørsteds Plads, building 345C
DK-2800 Kgs. Lyngby